Simultaneous measurements of liquid velocity and temperature for high pressure and high temperature liquid single phase flows

Fabrice Francois[a,*], Michel Kledy[b], Stéphane Barre[c], Henda Djeridi[c]

[a] *Institut de Recherches sur les Systèmes Nucléaires pour la Production d'Energie Bas Carbone – CEA/Cadarache 13108, St Paul Lez Durance Cedex, France*
[b] *ECM Technologies, 38029 GRENOBLE Cedex 2, France*
[c] *Laboratoire des Ecoulements Géophysiques Industriels, CNRS - Grenoble INP - Université de Grenoble-Alpes, Domaine Universitaire, 38400 St Martin d'Hères, France*

Forced convective boiling is of great interest for several applications in the power and process industry, parti-cularly in nuclear plants. Under certain nominal, incidental or accidental conditions, boiling crisis (Departure from Nucleate Boiling) may occur resulting in the melting of the heated surface. An accurate prediction of the conditions leading to the occurrence of this phenomenon is then essential. We believe that such an objective unreachable unless one provides a good and accurate description of the associated two-phase flow. To achieve this goal, local parameters e.g. void fraction, vapor and liquid velocities, liquid temperature…, need to be measured within the range of interest, which mainly concerns the high pressure and high temperature con-vective boiling flows. In this work, we only focus on the liquid velocity and temperature measurements and we propose to use thermal anemometry for performing such measurements. However, due to the high complexity of those flows, we have developed a two-steps strategy. Indeed, before using such an experimental technic for boiling flows, we need first to check the feasibility of this method for characterizing single-phase heated flows. Measurements for boiling flows will be performed in a second step, which is beyond the scope of the present paper. We applied the multiple overheating method for simultaneous measurement of the liquid velocity and the liquid temperature using a single sensor. If this methodology has already been used for gas flows measurements (Bestion et al., 1983; Barre et al., 1992, 1994), as far as we know, this work is the first attempt for liquid flows. We conducted experiments in a circular heated tube whose inner diameter and length are 19.2 mm and 3.5 m, respectively. The sensor (hot wire d~5 μm) has been operated with the Constant Current mode (CCA). To consider for temperature effect on velocity calibration, we proposed a new non-dimensional representation of the calibration curve. We also improve the frequency response of the probe using a digital compensation method. Preliminary tests for single-phase flows confirmed that it was possible to get very accurate measurements of mean and fluctuating liquid velocity profiles as well as mean temperature profiles. We have carefully analyzed the experimental uncertainties, which are close to 0.5 ˚C for the liquid temperature and ± 5% for the liquid velocity.

1. Introduction

When a liquid flows along a heated wall, nucleate boiling may occur if the wall heat flux is high enough. However, the resulting increase of the heat transfer coefficient is limited by the onset of the Departure from Nucleate Boiling (DNB) also known as the boiling crisis. This may cause severe damages including the meltdown of the wall. Predicting the thermal hydraulic conditions leading to DNB's occurrence is then a major industrial issue. Unfortunately, the physical mechanisms that may be responsible for this phenomenon are still not understood despite they have been continuously studied for more than sixty years. From a practical point of view, those conditions are usually determined using empirical correlations where the critical heat flux q_p is depending on other parameters like the pressure, the mass flux or the equilibrium quality, which are area-averaged quantities. As an example, for complex geometries like rod-bundles, those quantities are calculated using a sub-channel analysis code. Nevertheless, those correlations generally suffer from a lack of generality and consequently they cannot be used outside their range of validity.

Guelfi et al. (2005) have proposed a new approach - the so-called Local Predictive Approach that consists in developing empirical CHF correlations using local CFD calculated parameters instead of area-

---

[*] Corresponding author.
E-mail addresses: fabrice.francois@cea.fr (F. Francois), Stephane.barre@legi.grenoble-inp.fr (S. Barre), henda.djeridi@legi.grenoble-inp.fr (H. Djeridi).

averaged quantities. This scaling is expected to lead to a better consideration (i) for relations between boiling crisis and local structure of boiling flows and (ii) for parametric effects on DNB e.g. the axial shape profile or the cold wall effect. In order to achieve this goal, a necessary requirement is at least to use highly validated numerical tools for the local conditions calculations within the thermal hydraulic range of interest, which mainly concerns high pressure and high temperature convective boiling flows. This point is very sensitive since two-phase flows behave in a different way depending on the operative conditions and especially the pressure. Thus, for pressure greater than 7 MPa, Hösler (1968) has observed that at high void fraction, steam-water boiling flows are neither annular nor droplet flows but that they look like a froth flow. Francois et al. (2011) have also shown that in similar thermal hydraulic conditions, whatever the void fraction from subcooled to saturated flow, the two-phase flow was a bubbly emulsion where the liquid remains the continuous phase.

Characterizing the local flow structure in the range of interest is then an important step towards a correct two-phase flow understanding and modeling.

However, such experimental conditions make measurements difficult to perform and consequently there are few databanks on high pressure boiling experiments. For illustration, we tried to draw up an inventory of some available database (see Table 1) for convective boiling experiments. For each identified databank, the working conditions as well as the measurement techniques have been specified. When the working fluid is not steam/water, we have also indicated the equivalent pressure calculated using the vapor/liquid density ratio as scaling criteria. For low-pressure experiments, many parameters can be measured. Thus, Roy et al. (1997) have measured the void fraction, the liquid temperature but also the phasic velocities as well as the fluctuating components of the velocity and the temperature. However, for higher pressure, measurements are often limited to void fraction including sometimes the liquid and/or the wall temperature. The DEBORA databank (Garnier et al., 2001) is worthwhile being mentioned. Indeed, many local measurements including void fraction, liquid and wall temperature, gas velocity but also bubble diameters and interfacial area concentration have been performed. Freon R12 and Freon R134A were used as coolant fluids. Unfortunately, the liquid velocity has not been measured during those experiments. As a consequence, it is necessary to do many assumptions for analyzing the data, those assumptions being sometimes hard to justify. This study directly arises as a result from this observation.

Many experimental technics are available in order to measure the liquid velocity. One can cite for example the Laser Doppler anemometry (Roy et al., 1997), the particle image velocimetry (PIV) or particle-tracking velocimetry (PTV). But those technics require an optical access to the test section and they are often limited to very low values of the void fraction. More recently, Lemonnier and Julien (2011) have shown that Nuclear Magnetic Resonance (NMR) could be a good candidate for measuring the void fraction and the liquid velocity profiles in a two-phase flow with a good accuracy especially in the wall-region. Nevertheless, those tests have been performed in an adiabatic air–water flow and the relevance of this technic for boiling flows is still to be substantiated.

Up to now, thermal anemometry appears as a mature technology specifically for experiments involving monophasic gas flows (Comte-Bellot (1976), Bruun (1995)) including supersonic flows (Bestion et al. (1983), Bonnet and Knani (1988), Smits and Muck (1984)) or transonic flows (Barre et al. (1992), Barre et al. (1994)). This method is also widely used in isothermal liquid monophasic flows (Resch and Coantic (1969), Bruun (1996)). Recently, Hasan et al. (1992) used thermal anemometry to measure the liquid velocity and temperature in non-isothermal flow of Freon R113. They used a micro sensor consisting of 3 hot-film probes (diameter equal to 25 μm and sensitive length equal to 440 μm). Two of these probes, which were powered using a constant temperature anemometer, were used to measure the axial and radial

Table 1

Inventory of experimental database in boiling convective flows - U_L, T_L, T_p, α_G, U_G, U_G, d_B correspond respectively to the liquid velocity, the liquid temperature, the temperature of the heated wall, the void fraction, the gas velocity, the bubble diameter, and the interfacial area concentration. - $\overline{u'^2}$, $\overline{v'^2}$, $\overline{t'^2}$, $\overline{v't'}$, $\overline{u'v'}$ correspond to axial and radial velocity fluctuations, temperature fluctuations, and cross fluctuations. * According to Francois et al. (2011).

	Data bank	Fluid	Geometry	Experimental pressure (bar)	PWR corresponding pressure (bar)	Local measurements	Measurement techniques
High pressure *	BFBT,Inoue et al. (1995)	Water	Rod bundle	1–86	1–86	α_G	X-Ray
	DEBORA,Garnier et al.(2001)	R12/ R134a	Cylindricalduct	14–30	100–180	α_G, d_B, U_G, T_L, T_p	Optical probes, micro- thermocouples
	Perez and Hassan (2010)), Hassan (2015)	HFE −301	Rectangular duct	1–16	10–140	T_p, U_L, $\overline{u'v'}$, $\overline{u'^2}$, $\overline{v'^2}$	PTV
Low pressure	Dix(1971)	Freon R114	Cylindrical duct	3	25.5	α_G, T_L	Cold & hot wire anemometry
	ASU,Roy et al. (1997)	Freon R113	Annular duct	3	24.5	α_G, d_B, U_G, U_G, U_L, T_L, , $\overline{u'^2}$, $\overline{v'^2}$, $\overline{t'^2}$, $\overline{v't'}$, $\overline{u'v'}$	Optical probes, micro- thermocouples, cold wire, PIV
	Situ et al. (2004)	Water	Annular duct	1–2	1–2	U_G, α_G, a_i	Conductivity probe
	KAERI, Lee et al. (2002)	Water	Annular duct	1.5–2		U_G, U_L, α_G, d_B, a_i	Conductivity probe, pitot probe
	SUBO,Yun et al. (2010)	Water	Annular duct	1.5–2	1.5–2	α_G, d_B, U_G, U_L, T_L, T_p	Optical probes, micro- thermocouples, pitot probe

components of the liquid velocity. The authors set the operating temperature 30 °C above the liquid temperature, which corresponds to a temperature 10 °C below the saturation temperature in order to avoid nucleate boiling on the probes while insuring a good sensitivity for their measurements. The third probe was used to measure the liquid temperature. For such measurements, the anemometer was coupled to an electronic compensation circuit in order to improve the bandwidth of the temperature measurement. Two interesting conclusions can be pointed out from this study. First, there is a great impact of the non-isothermal effects on the velocity measurement accuracy that has to be taken into account through an adapted calibration process. Unfortunately, this process is not accurately described by Hasan et al. (1992) in their paper. Second, the size of the sensor prevents the authors to perform measurements close to the heated wall, the nearest measurements being located at 1 mm from the wall. Despite those drawbacks, we have chosen this experimental method for the reasons set out below:

- This technic doesn't require any optical access to be used, contrary to PIV or PTV,
- A very high spatial resolution can be achieved using very small sensors whose diameters can be low as 2.5 μm,
- This technic allows accessing the liquid velocity but also the liquid temperature and the phase indicator function.

To achieve this goal, we have proposed a two-steps strategy. Indeed, due to the high complexity of boiling flows, especially for high pressure and high temperature conditions, we believed that it is was necessary to introduce two stages in this work. First, the feasibility of this method for characterizing single phase heated flows will be checked. In particular, an original method will be proposed to access simultaneously the mean liquid velocity as well as the liquid temperature. In a second step which is beyond the scope of this work, the use of this technic for boiling flows will be studied. This paper whicht only focuses on the first stage is organized as follows. In Section 2, the experimental facility named DEBORA where the tests have been performed as well as the operating conditions will be set out in details. The measurement technic is described in Section 3. An overview of the experimental results for single-phase adiabatic and heated flows is given in Section 4. Special attention will be given on mean liquid velocity and temperature measurements but also on turbulent quantities.

2. Experimental setup and operating conditions

As experiments performed with steam-water at high pressure would be expensive, Refrigerant 134 (R134A) has been used for simulating the operating conditions of a pressurized water reactor (PWRs). Thanks to the physical properties of R134A, it becomes possible to reproduce flow characteristics similar to those encountered in water under PWR conditions but at much lower pressure, temperature and heat fluxes.

2.1. Scaling criteria

The overall parameter ranges in R134A are determined by the following criteria (Stevens and Kirby, 1964):

- Almost identical geometry (cross-section shape, heated area, cross-sectional area).
- Same vapor/liquid density ratio to determine the R134A system pressure P:

$$\left(\frac{\rho_f}{\rho_g}\right)_{water} = \left(\frac{\rho_f}{\rho_g}\right)_{R134A} \tag{1.1}$$

where ρ_f and ρ_g are the saturated liquid density and the vapor density, respectively.

- Same Weber number (We) to determine the R134A mass flux G

$$\left(\frac{G^2 R}{\rho_f \sigma}\right)_{water} = \left(\frac{G^2 R}{\rho_f \sigma}\right)_{R134A} \tag{1.2}$$

where σ and R are the surface tension and the radius of the pipe, respectively.

- Same boiling number (Bo) to calculate the corresponding heat flux q_p in the R134A facility:

$$\left(\frac{q_p}{G h_{fg}}\right)_{water} = \left(\frac{q_p}{G h_{fg}}\right)_{R134A} \tag{1.3}$$

where h_{fg} is the latent heat of vaporization.

- Same inlet equilibrium inlet quality $x_{eq,in}$ to determine the R134A inlet temperature:

$$(x_{eq,in})_{water} = (x_{eq,in})_{R134A} \tag{1.4}$$

Or

$$\left(\frac{h_{l,in} - h_f}{h_{fg}}\right)_{water} = \left(\frac{h_{l,in} - h_f}{h_{fg}}\right)_{R134A} \tag{1.5}$$

where $h_{l,in}$ is the liquid inlet specific enthalpy and h_f is the specific enthalpy of the saturated liquid.

These similarity criteria lead to the flow characteristics of the R134A loop listed in Table 2.

2.2. The test facility

All the tests have been performed on a test facility named DEBORA (CEA/Grenoble). This experimental rig which uses Freon (R12 when being designed then Freon R134A) allows to control the four following parameters: pressure P, inlet temperature T_{in}, mass velocity G and heat flux q_p in the range given in Table 2.

The loop is designed with two independent circuits: the test section circuit and the coolant storage circuit, which is not represented on Fig. 1 but whose a whole description is given by Garnier et al. (2001). The test section circuit is composed of:

- A pump (2) with a flow rate of 4.5 kg/s for a 100 m head, the flow rate in the test section being controlled by regulating valves,
- A 30 kW preheater (7) which imposes the inlet temperature of the test section,
- A test section (8) which is electrically heated by two direct current generators (100 kW each with a maximum intensity of 1250 A),
- A direct contact condenser (9) which mixes the flow at the outlet of the test section and the flow at the outlet of the parallel heat exchanger (4) in order to obtain a liquid Freon flow at the inlet of the second heat exchanger (5)
- A heat exchanger (4) (200 kW, 6 kg/s) which is installed in parallel with the test section in order to decrease the Freon temperature from 60 °C to 30 °C at the inlet of the pump
- A heat exchanger (5) (70 kW, 1.5 kg/s) in order to decrease the

Table 2
Water incidental conditions and corresponding R134A flow characteristics; corresponding ranges are calculated using the scaling criteria (1.2) to (1.5).

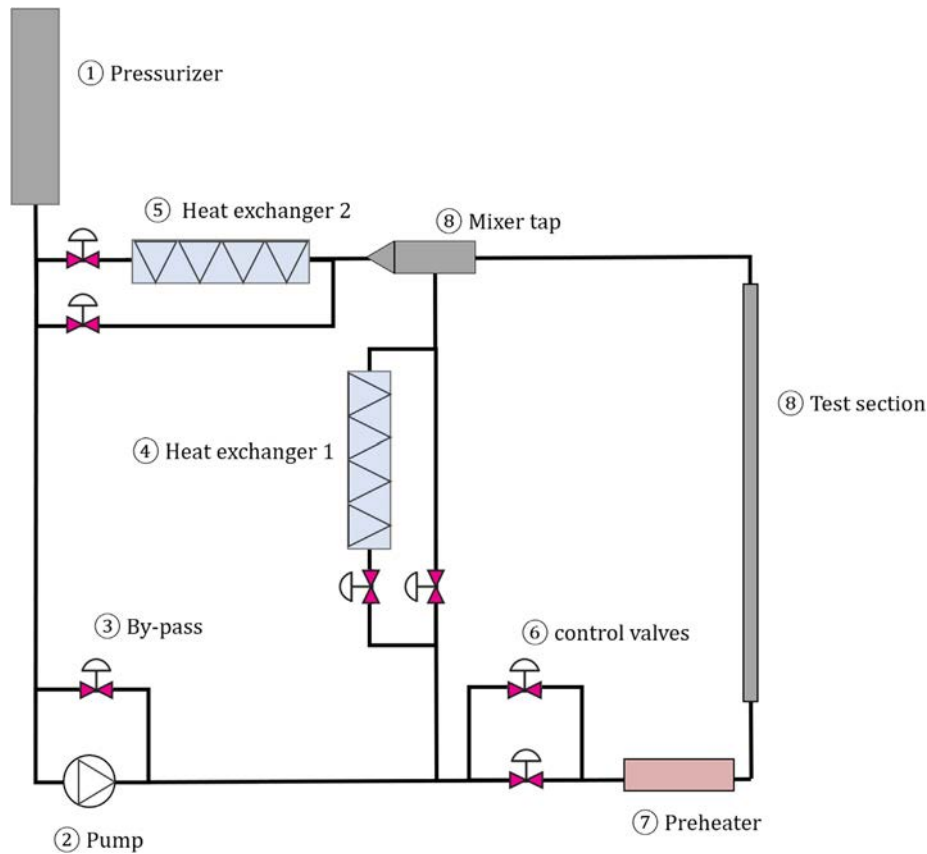| Control parameters	Water	R134A
Exit pressure (MPa)	10 to 16	1.4–2.6
Mass flux (kg.m-2.s-1)	500 to 5000	500–5000
Heat flux (MW.m-2)	0.5 to 3	0.01–0.20
Inlet temperature (°C)	50 to 320	20–80
Equilibrium exit quality	−0.3 to 0.5	−0.3–0.5

Fig. 1. General view of the test loop. The flow direction in the test section is upward vertical.

Freon temperature from 60 °C to 40 °C at the exit of the condenser

- A pressurizer (**1**) (0.14 m³, 6 KW) to impose the pressure at the outlet of the test section (maximum pressure is 3 MPa).

2.3. Measurements of the control parameters

Classical pressure sensors based on capacity variations measure the pressure in the test section. These sensors have ± 0.5% accuracy. While pressure measurements are performed at the inlet and the outlet of the test section (see Fig. 2), there are no pressure measurements along the test section.

The temperature at the inlet and the outlet of the test section (Fig. 2) are performed using Platinum sensors (two at the inlet and two at the outlet). After calibration and accounting for the whole measurement chain, the temperature measurement accuracy is estimated to be ± 0.2 °C.

A Coriolis flowmeter measures the mass flow rate over the following range: 0.17 kg/s up to 1,7 kg/s with a relative accuracy of ± 0.1%. Due to the influence of the temperature, it is necessary to calibrate the device for several temperature from 20 °C up to 80 °C in order to cover the whole range of parameters.

The electrical power, which is injected in the test section, is determined by measuring both the voltage and the intensity over the test section. The voltage is measured by means of direct connections to the test section boundaries whereas the intensity is measured using a magnetic intensity converter located close to the electrical power rectifier. The power measurement is estimated to have an accuracy level of about ± 3%.

2.4. The test section

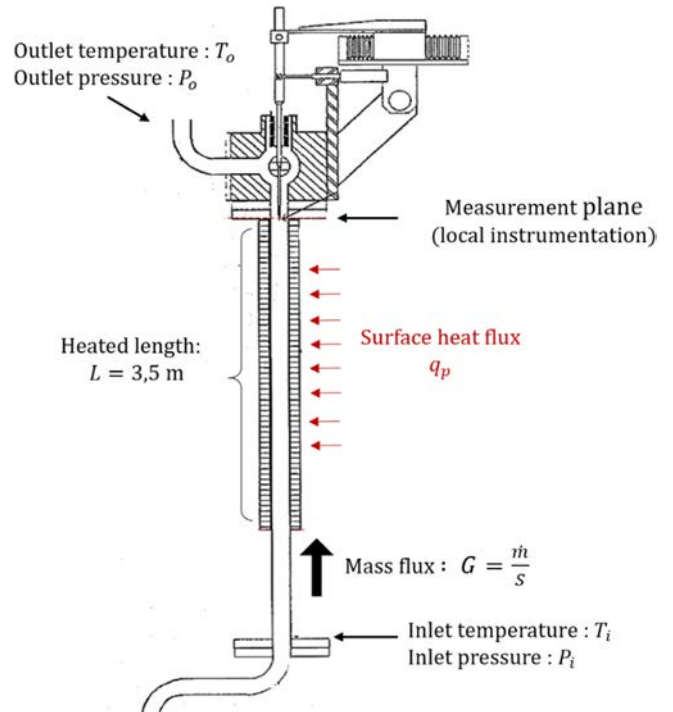The test section is a single vertical tube with a circular cross section.

Fig. 2. General view of the test section.

It is made of Stainless Steel (316TI). The internal diameter is 19.2 mm ± 0.2 mm and the external diameter is 21.2 mm ± 0.05 mm. The length of the tube is 3.485 m and it can be heated by Joule effect in whole or in part thanks to two power rectifiers connected

4

to the top and the bottom of the test section and who can deliver an electrical current of 1250 at a voltage value of 80 V. The test section is thermally insulated on its external face with a layer of rock wool 6 cm thick, so that the power losses can be neglected.

Thanks to ultrasonic sensors, the thickness of the tube was measured along the vertical axis of four angular positions (every 90°) with 100 mm step. Electrical resistance is also measured every 100 mm to check the axial and the azimuthal uniformity of the heat flux. The maximum variations of the local electric resistance is 0.35% of the mean value.

Local measurements are performed at the outlet of the test section using a specific device able to move a probe along one diameter (the flow is assumed to be axisymmetric). Many different measurement sensors can be connected to this moving system like thermocouple, optical probes (Garnier et al., 2001) or hot-wires in this work. By an adapted specific calibration procedure, which depends on the sensor, it is possible to determine the accuracy of the probe positioning. In this study, the accuracy of the positioning is 100 μm whereas the moving resolution is close to 10 μm.

The instrumentation of the test section only concerns the wall temperature measurements. Those temperatures are measured using three platinum micro-probes (Pt100, JUMO Platinum Temperature sensors) glued to the external face of the heated tube. They are located 0.02 m before the end of the heated length and they are distributed on the ring every 120°. Those probes were gauged *in situ* during adiabatic isothermal liquid single phase tests being relative to the Platinum probe used for measuring the fluid temperature at the outlet of the test section.

The uncertainty of wall temperature measurements is estimated to be equal to 0.6 °C. Table 3 summarizes the accuracy of the measured parameters.

In order to guarantee the quality of the measurements, it is of first importance to check the stability of the boundary conditions, especially in case of long-time measurements. The temporal evolution of the control parameters (inlet temperature, outlet pressure, mass flow rate and electrical power) has been registered during seven hours for a given set of thermal hydraulic conditions. The fluctuations of those parameters remains lower than 0.5% for the pressure, the mass flow rate and the electrical power whereas the fluctuation of the inlet temperature is lower than 0.1 °C. Results are summarized in Table 3.

3. Hot wire anemometry in DEBORA experimental set-up

3.1. Operating principle

The principle of thermal anemometry is to put one or more elements (sensors) heated by Joule effect in an incident flow. Du to heat exchanges between the sensor and the fluid, the heated element is cooled. When thermal balance (steady state) is reached, the power produced by the Joule effect is completely evacuated by convection and the temperature of the wire stabilizes at a so-called equilibrium temperature T_w. The electrical resistance of the wire R_w is expressed as:

$$R_w = R_a \left[1 + \alpha_a (T_w - T_a) \right] \tag{1.6}$$

Table 3
: Measurements uncertainties.

	Sensor type	Accuracy	Stability
Inlet Temperature	Platinum sensor	± 0. 2°C	± 0. 1°C
Outlet temperature	Platinum sensor	± 0. 2°C	± 0. 1°C
Mass flow rate	Coriolis flowmeter	± 0.1%	± 0.5%
Wall temperature	Micro-Platinum sensor (JUMO)	± 0. 6°C	± 0. 1°C
Inlet pressure	Pressure sensor	± 0.01bar	± 0.5%
Outlet pressure	Pressure sensor	± 0.01bar	± 0.5%
Heat Power	Voltmeter/ammeter	± 3%	± 0.5%

where T_a, R_a, T_w and α_a denote a reference temperature, the electrical resistance of the wire at temperature T_a and the coefficient of thermal sensitivity of the wire, respectively. α_a is defined by the following relation:

$$\alpha_a \triangleq \frac{1}{R_a} \frac{\partial R_w}{\partial T} \tag{1.7}$$

Sensors are thin metallic wires with typical diameter of 0.5–5 μm and typical length of 0.1–1 mm made of several materials as tungsten, platinum or platinum–rhodium. For liquids such as water, hot-film sensors are used. They consist of a thin platinum film deposited by sputtering on a quartz support. An additional quartz coating then protects the film from electrochemical effects. The typical diameter is 20–70 μm and sensitive length generally varies from 200 μm to 1.3 mm. Since these characteristics make them more suitable for use in liquid flow, their important size lead to lowest performances in terms of spatial and temporal resolutions than for the wires. Two operating modes are conventionally used to supply the measurement sensor. The first one named the Constant Current operation (CCA) consists of injecting a constant electrical current into the sensor. This operating mode is conventionally used to perform temperature measurements. The second one named Constant temperature (or resistance) operation (CTA) consists in maintaining the temperature of the probe at a constant value by means of an electronic feedback circuit. This operating mode is conventionally used to perform velocity measurements.

Under transient conditions, the energy balance over the sensor can be written as:

$$m_w C_{pw} \frac{\partial T_w}{\partial t} = R_w I^2 - h S_w (T_w - T_0) \tag{1.8}$$

where m_w, C_{pw}, T_w, R_w, I, T_0, h and S_w denote the mass of the wire, its specific heat capacity, the temperature and resistance of the sensor, the electrical current in the sensor, the fluid temperature, the heat exchange coefficient, and the heat exchange surface between the wire and the fluid defined as:

$$S_w = \pi d l \tag{1.9}$$

where l and d correspond to the sensitive length and the diameter of the sensor respectively.

Under steady-state conditions, equation rewrites as:

$$R_w I^2 = h S_w (T_w - T_0) \tag{1.10}$$

The heat exchange coefficient h is expressed as a function of the Nusselt number Nu_w :

$$Nu_w \triangleq \frac{hd}{\lambda} \tag{1.11}$$

where λ is the thermal conductivity of the fluid. Classically, Nusselt number may depend on various dimensionless parameters. In the present experimental thermal hydraulic conditions, the Nusselt number mainly depends on both the Reynolds and Prandtl numbers defined as:

$$Re_w \triangleq \frac{\rho U d}{\mu}; \; Pr \triangleq \frac{\mu C_p}{\lambda} \tag{1.12}$$

where μ and ρ correspond to the dynamic viscosity and the density respectively, and U is the incident velocity of the fluid. In the case of wire infinite in length, Kramers (1946) proposes the following relation to estimate the Nusselt number:

$$Nu_w = 0.42 Pr_f^{0.42} + 0.57 Pr_f^{0.33} \sqrt{Re_{w,f}} \tag{1.13}$$

where the index f means that the thermo-physical properties are evaluated at the film temperature, which is defined by:

$$T_f \triangleq \frac{T_w + T_0}{2} \tag{1.14}$$

The range of validity for the correlation of Kramers (1946) is:

$$\begin{cases} 0.01 < Re_w < 10^4 \\ 0.71 < Pr_f < 10^3 \end{cases} \tag{1.15}$$

By combining equations, and, we obtain the following expression for R_w :

$$R_w = \frac{R_0}{1 - \frac{\alpha_a R_a I^2}{Nu_{w,f}\pi l \lambda_f}} \tag{1.16}$$

Thus, for low values of the electrical current I (cold wire mode), the resistance of the wire R_w is close to R_0 which means that the temperature of the wire is very close to the fluid temperature ($T_w \sim T_0$). On the other hand, for higher values of the current I, the temperature of the wire increases. The sensor operates in hot wire mode and the resistance R_w depends on both the temperature of the fluid T_0 (term R_0 in Eq. (1.16)) and the velocity through the Nusselt number $Nu_{w,f}$ in Eq. (1.16). It is convenient to characterize the operating temperature of the sensor to introduce the wire overheat ratio a_w defined as:

$$a_w \triangleq \frac{R_w - R_0}{R_0} \tag{1.17}$$

Which can also be written:

$$a_w = \alpha_0 (T_w - T_0) \tag{1.18}$$

It appears that in order to get accurate measurements of both the liquid velocity and temperature profiles using hot wires on DEBORA facility, it is important to develop an adapted and specific strategy.

3.2. Strategy development for velocity and temperature measurements in DEBORA facility

3.2.1. Choice of the sensors

Since Freon R134A is an excellent electrical insulator ($\rho_{elec} > 10^8 \ \Omega.m$), it is possible to use wire sensors whose main advantage is in their small size (good spatial and temporal resolution). Due to its high thermal sensitivity coefficient compared to other materials, Tungsten probes were chosen.

During our experiments, we used hot-wire probes but also film probes, despite their lower spatial and temporal resolution. Indeed, they are classically used for measurements in liquid medium because of their robustness. It therefore seemed appropriate to test them in order to quantify the impact of a weak resolution on the quality of measurements and especially in the region near the heated wall. All those sensors have been manufactured by DANTEC ®. The geometries of the probes are given below:

- Hot wire probes : (i) hot wire 5 μm diameter and 1.25 mm length and (ii) hot wire 2.5 μm diameter and 700 μm length.
- Hot film probes : 70 μm diameter and 1.25 mm length

Table 4 summarizes the characteristics of the probes that were used during the present work:

The theoretical cut-off frequencies of those probes have been calculated for the following thermal hydraulic conditions: fluid Freon R134A, overheat ratio $a_w = 0.1$, liquid temperature equal to 20 °C and liquid velocity equal to 2 m/s.

Those frequencies are equal to 5 kHz and 20 kHz for the 5 μm and

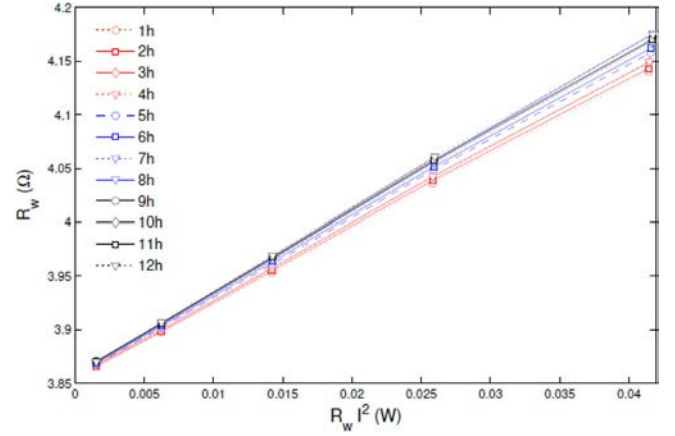**Fig. 3.** Evolution of the calibration curve $R_w(R_w I^2)$ as a function of time.

2.5 μm diameter wire probes respectively, whereas the cut-off frequency of the film probe is close to 200 Hz. It should be noticed that the theoretical cutoff frequencies are lower for airflows where, for the same thermal hydraulic conditions than below, the theoretical cutoff frequency of a wire probe (5 μm diameter) is close to 200 Hz. This is due to a better convective exchange in Freon.

CCA operation was used to perform measurements and in order to increase the bandwidth, a frequency compensation method is classically used. This can be done either analogically, using real-time compensation electronics (Hasan et al. (1992)), or a posteriori using digital signal processing methods (Wroblewski and Eibeck (1991), Tagawa et al. (1998), Khine et al. (2013)). The whole measurement chain is detailed in Klédy (2018).

3.2.2. Probes aging issues

During preliminary tests, we noticed a fast drift of the calibration curves as shown on Fig. 3 for Tungsten wires. Actually, the slope of the curve $R_w(R_w I^2)$ is continuously decreasing in a monotonic way.

These results suggest a possible degradation of the sensor surface condition. This hypothesis was checked by characterizing the wire's surface condition using an Electronic Scanning Microscope (SEM). Fig. 4 compare the evolution of the surface condition of a Tungsten wire before and after immersion during few hours in a Freon R134A flow.

A possible explanation for this highly visible alteration is based on a chemical interaction between the Tungsten the wire is made of and the Fluorine which is contained in the R134a, the Fluorine being known as a powerful oxidant. As film probes were not impaired by Freon, we decided to coat the Tungsten wire probes with a thin layer of Sapphire (Al_2O_3) in order to minimize the wire characteristics changes. The deposit was made using the so-called ALD (Atomic Layer Deposition) process by CEA/Liten in Grenoble (France). Some tests have shown that a thickness of 20 nm was sufficient to properly protect the probe. Before coating the probe, the drift of the wire resistance R_w was about 17% for a half-day test (Fig. 3) whereas after coating the drift is lower than 3% for a one-day test.

3.2.3. Multiple overheats method

As shown by Eq. (1.16), measuring both the liquid velocity and

Table 4
Characteristics of the various probes (DANTEC) used in this study. The values of the physical properties are given at 20 °C - * is related to Quartz properties.

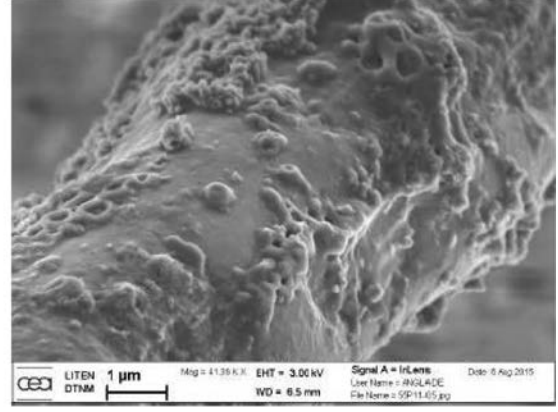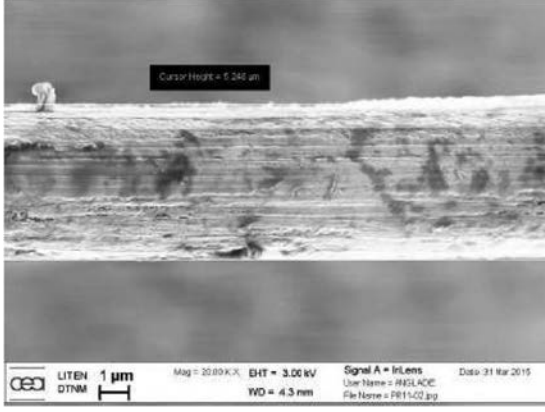| Probe	Material	d (μm)	l (mm)	α_{20} (K^{-1})	R_{20} (Ω)	ρ_w (kg.m^{-3})	$C_{p,w}$ (J.kg^{-1}.K^{-1})	λ_w (W.m^{-1}.K^{-1})
Wire	Tungsten	5	1.25	0.0036	3.5	19,300	130	190
Wire	Tungsten	2.5	0.7	0.0036	3.5	19,300	130	190
Film	Quartz + Nickel	70	1.25	0.0045	8	265*	790*	1.5*

Fig. 4. Visualization of the surface condition of a 5 μm diameter Tungsten wire (uncoated) using a scanning electron microscope - (left) new probe - (right) probe immersed in a Freon R134a flow during several hours.

temperature requires at least two different sensors overheats. Actually, the wire must be powered by a low current (cold wire mode) for temperature measurements whereas the supply current must be as high as possible (hot wire mode) for velocity measurements. In such an approach, velocity measurement is impacted by the accuracy of the temperature measurements, when the injected current is low. To overcome this limitation, the multiple overheats method was used. Originally developed by Corsin (1947), this method has largely been used by Bestion et al. (1983), Bonnet and Knani (1988), Barre et al. (1992) and Barre et al. (1994) and more recently by Ndoye (2008) to perform calibrations within single-phase gas flows. But, to our knowledge, this is the first time that this method is used in a liquid flow.

The measurement of the liquid velocity and temperature is based on Eq. (1.16), which provides a relationship between the sensor resistance R_w and the electrical power $R_w I^2$ that is injected in the sensor:

$$R_w = R_0 + \frac{\alpha_a R_a}{Nu_{w,f} \pi l} \frac{R_w I^2}{\lambda_f} \quad (1.19)$$

The multiple overheats method consists of successively injecting several currents into the wire for an imposed liquid velocity and temperature. For each value of the injected current, the equilibrium resistance of the wire R_w and the dissipated power $R_w I^2$ are measured. According to Eq. (1.19) and if we assume that the Nusselt number do not depend on the overheat ratio, the curve $R_w(R_w I^2)$ must be linear. R_0 is the intercept and only depends on the liquid temperature T_0. The slope is a function of the Nusselt number, and therefore of the fluid velocity. By carrying out this procedure for several velocity/temperature samples, it becomes possible to calibrate the probe by connecting the fluid temperature T_0 to the wire recovery resistance R_0, and the Nusselt number Nu_{w_f} to the incident velocity of the flow U and to the temperature of the liquid T_0. During the effective measurement process, this procedure will be reversed in order to obtain both the velocity and the temperature from the calibration curve defined by the relation (1.19).

The calibration is directly performed within the test section. One flow condition which is characterized by one temperature and one mass flux is imposed. The flow is assumed to be adiabatic and its temperature T_0 is measured using both Platinum probes located at the inlet and the outlet of the tube, respectively. The difference between those two measurements is lower than 0.1 ˚C. The hot-wire probe is located on the axis of the tube. The liquid velocity is given by the correlation of Zagarola and Smits (1998) whose range of validity is $98. \, 10^3 < Re < 35. \, 10^6$. According to the authors, the accuracy of the correlation is equal to ± 0.55%:

$$\frac{U_c}{u^*} = 5.629 \log(Re\sqrt{f}) + 3.742 \quad (1.20)$$

where u^*, Re and f are the friction velocity, the flow Reynolds number and the friction factor respectively.

The friction velocity u^* is defined as:

$$u^* \triangleq \sqrt{\frac{\tau_w}{\rho_0}} \quad (1.21)$$

Where τ_w and ρ are the wall shear stress and the liquid density. The subscript 0 indicates that the thermophysical properties are evaluated at the temperature T_0. τ_w can be expressed as:

$$\tau_w = \frac{f}{8} \frac{G^2}{\rho_0} \quad (1.22)$$

The flow Reynolds number Re is defined as:

$$Re \triangleq \frac{GD}{\mu_0} \quad (1.23)$$

where μ is the kinematic viscosity of the liquid.

The friction factor f is expressed as:

$$\frac{1}{\sqrt{f}} = 1.884 \log(Re\sqrt{f}) - 0.331 \quad (1.24)$$

Since the temperature and the velocity at the probe location are known, it is possible to calculate the Reynolds number of the wire $Re_{w,0}$ defined as:

$$Re_{w,0} = \frac{\rho_0 U_c d}{\mu_0} \quad (1.25)$$

For those specific flow conditions that are now characterized by T_0 and $Re_{w,0}$, we plot the curve $R_w = f(R_w I^2/\lambda_f)$ by injecting for this flow condition several values of the injected current I. The film temperature T_f can be directly determined using Eqs. (1.6) and (1.14):

$$T_f \triangleq \frac{T_w + T_0}{2} = \frac{1}{2}\left[\frac{1}{\alpha_{20}}\left(\frac{R_w}{R_{20}} - 1\right) + (T_0 + 20)\right] \quad (1.26)$$

Fig. 5 gives an example of typical curve that can be obtained for several values of T_0 and $Re_{w,0}$.

As expected, for a given set of flow conditions, there is a linear relation between R_w and $R_w I^2/\lambda_f$, which confirms that the Nusselt number (Eq. (1.19)) does not depend on the overheat ratio e.g. the injected current. We can also notice that the recovery resistance R_0 only depends on the fluid temperature but not on the fluid velocity. This result will simplify the calibration and measurement process.

The experimental curves are linearly interpolated and the slope of those curves gives access to the Nusselt number Nu_w according to Eq. (1.19):
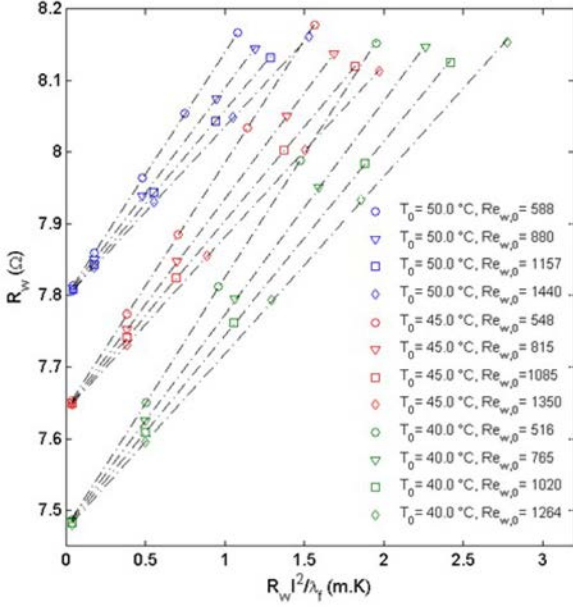
Fig. 5. $R_w = f\left(\frac{R_w I^2}{\lambda_f}\right)$ for several values of T_0 and $Re_{w,0}$. Measurements have been performed using a hot-film probe from DANTEC®.

$$Nu_w(Re_{w,0}, T_0) = Nu_{w,0} = \frac{\alpha_{20} R_{20}}{A\pi l} \qquad (1.27)$$

where A is the slope of the curve $R_w(R_w I^2/\lambda_f)$.

We can also observe on Fig. 5 that for a given temperature, the slope A decreases when the Reynolds number $Re_{w,0}$ increases. This can be explained by an enhancement of the convective heat transfer around the wire which naturally leads to an increase of the Nusselt number and consequently a decrease of the slope. The calibration curves for the liquid temperature and velocity can then be obtained. As the recovery resistance does not depend on the velocity as mentionned before, we only obtain one single curve (see Fig. 6). In contrast, Fig. 7 shows a batch of calibration curves for the velocity $Nu_{w,0}(Re_{w,0})$, each of them depending on the liquid temperature T_0. For a given liquid temperature,
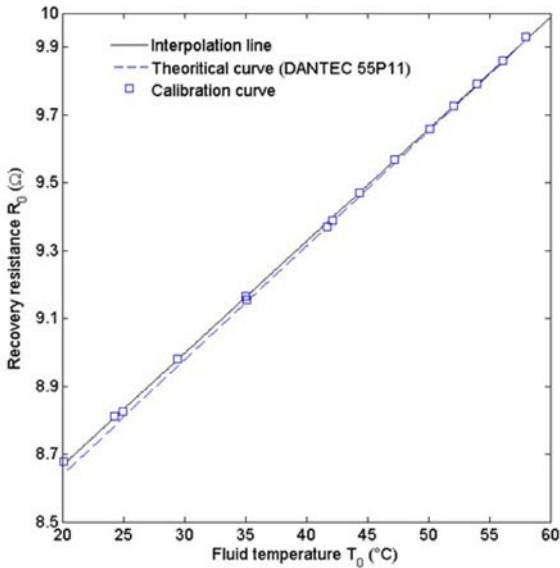

Fig. 6. Calibration curve for the liquid temperature. Measurements have been performed with a ho-film probe from DANTEC®. The dashed line corresponds to the theoretical relation between the electrical resistance and the temperature provided by the manufacturer.
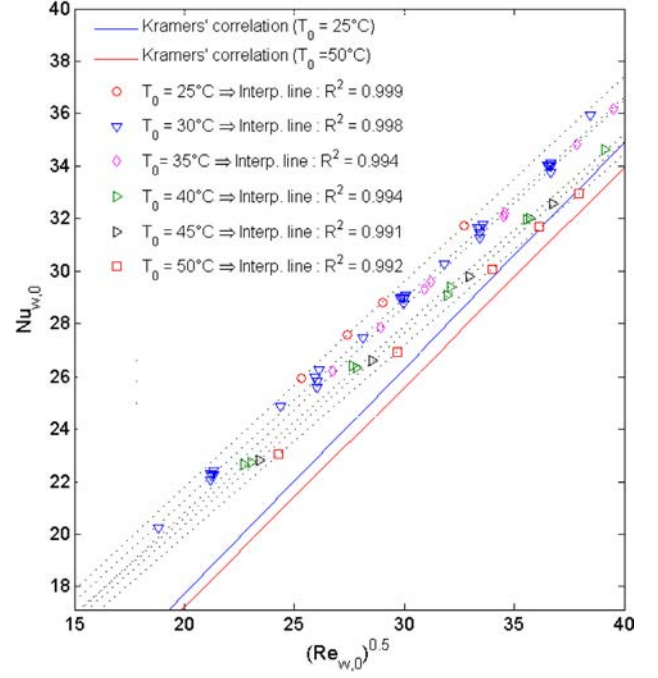

Fig. 7. Calibration curves for the liquid velocity. Measurements have been performed with a hot-film probe from DANTEC® d = 70 µm for several fluid temperatures. The liquid velocity ranges from 1 to 3 m/s. The liquid temperature varies between 20 and 50 °C. The solid line are related to the correlation of Kramers correlation (1946) - equation.

the Nusselt number $Nu_{w,0}$ seems to linearly vary with the square root of the Reynolds number $Re_{w,0}$. Nusselt numbers predicted by Kramers (1946) (Eq. (1.13)) were also plotted on the same figure. There is a good agreement with our experimental results (the maximum deviation being close to 15% as shown on Fig. 7), despite this correlation being valid for a wire with an infinite length.

In order to take into account for the temperature effect on the velocity calibration curves, since the ratio $Nu_{w,0}/Pr_0$ seems to be independent from the temperature as shown on Fig. 8, we propose to express the velocity calibration curve as follows:

$$Re_{w,0}^{0.5} = A_{Nu} + B_{Nu} \frac{Nu_{w,0}}{Pr_0} \qquad (1.28)$$

Fig. 9 displays the calibration curve which is obtained using Eq. (1.28). We can observe that whatever the liquid temperature, all the experimental data gather on a single linear curve. This new approach thus makes it easier to take into account for the temperature effect on the velocity calibration process

3.2.4. Procedure for measuring time-averaged quantities

The procedure for simultaneouly measuring the time-averaged liquid velocity U_L and temperature T_L directly arises from the calibration procedure. It is organized in four steps. The first one consists on injecting several values of the electrical current into the probe. From a practical point of view, five values are enough to get an acceptable accuracy for linear interpolation of the curves $R_w(R_w I^2/\lambda_f)$. The time duration of each test corresponding to each overheat ratio is 3 min. It is then possible in a second step to deduce from those experimental plots, the Nusselt number $Nu_{w,0}$ as well as the recovery resistance R_0, by determining the slope and the origin of the previous curves, respectively. The third step leads to the direct determination of the liquid temperature $T_L(r)$ by using the calibration curve for temperature $T_0(R_0)$. Finally, the velocity $U_L(r)$ is determined by deducing the Reynolds number $Re_{w,L}$ from the velocity calibration curve:
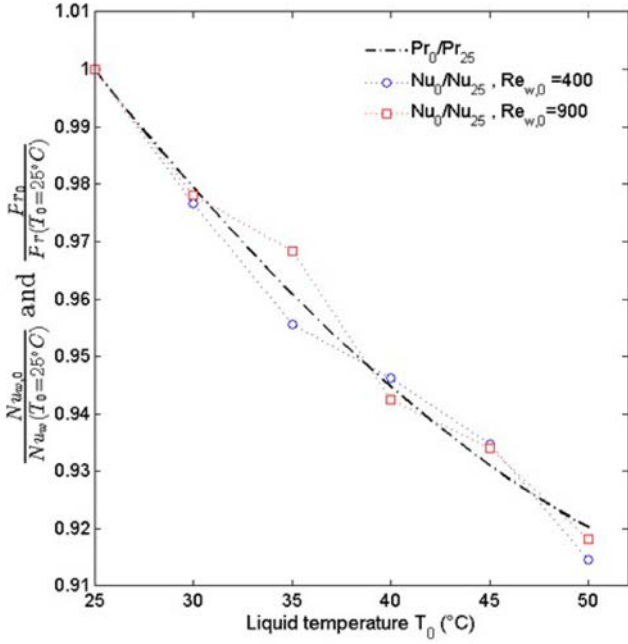
Fig. 8. Variation of experimental Nusselt numbers with liquid temperature for different values of the Reynolds number. Comparison with the evolution of Prandtl numbers in the same conditions. Nusselt and Prandtl numbers are normalized by their value calculated at 25 °C. Measurements have been performed using a hot-film probe.
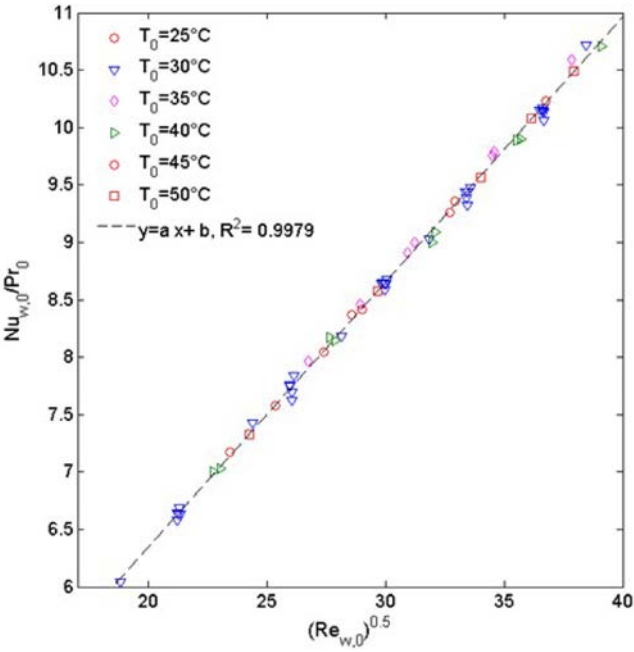

Fig. 9. Velocity calibration curves obtained for several fluid temperatures. Meausrments have been performed using a hot-wire probe d = 5 μm.

$$\frac{Nu_{w,0}}{Pr_0} = f\left(\sqrt{Re_{w,0}}\right) \tag{1.29}$$

We can deduce the liquid velocity using the Reynolds number définition :

$$Re_{w,L} \triangleq \frac{\rho_L U_L(r) d}{\mu_L} \tag{1.30}$$

where μ_L and ρ_L are the kinematic viscosity and the liquid density

calculated at the local liquid temperature $T_L(r)$.

The duration of the measurement process for one radial location in the tube is 20 mn which implies that the whole measurement process for one radial profile (made of twenty radial locations) is about 6 to 7 h.

3.2.5. Procedure for measuring turbulent quantities

In order to measure the turbulent fluctuations of velocity and temperature, we use the fluctuation diagram method, which was initially developed by Corrsin (1947) for single phase gas flows at low velocity. Kovasznay (1953) has extended this approach to the case of supersonic flows. We introduce here the basic principle.

When the injected current in the probe I is kept constant, the instantaneous probe voltage $e_w(t)$ is a function of both the fluid velocity $U_L(t)$ and the fluid temperature $T_L(t)$:

$$e_w(t) = f[U_L(t), T_L(t)] \tag{1.31}$$

By differentiating Eq. (1.31), we obtain:

$$de_w(t) = \left(\frac{\partial e_w}{\partial U_L}\right)dU_L + \left(\frac{\partial e_w}{\partial T_L}\right)dT_L = \left(\frac{\partial e_w}{\partial U_L}\right)u^{'} + \left(\frac{\partial e_w}{\partial T_L}\right)t^{'} \tag{1.32}$$

Which can also be rewritten as:

$$\frac{de_w}{e_w} = F\frac{u^{'}}{U_L} + G\frac{t^{'}}{T_L} \tag{1.33}$$

where F and G are the velocity and the temperature sensitivity coefficients respectively defined as

$$F \triangleq \frac{\partial \ln(e_w)}{\partial \ln(U_L)} \tag{1.34}$$

And

$$G \triangleq \frac{\partial \ln(e_w)}{\partial \ln(T_L)} \tag{1.35}$$

Following the pionnering work of Morkovin (1956), we can derive from equations (1.34) and (1.35) the following expressions of those sensitivity coefficients:

$$F = A_w \frac{\partial \ln(Nu_w)}{\partial \ln(Re_w)} \tag{1.36}$$

And

$$G = -K + A_w\left[1 - K + n + (k - m)\frac{\partial \ln(Nu_w)}{\partial \ln(Re_w)}\right] \tag{1.37}$$

where the parameters K and A_w are defined respectively as :

$$\begin{cases} K = \frac{\alpha_0 T_0}{1 + a_w} \\ A_w = \frac{a_w}{1 + a_w} \end{cases} \tag{1.38}$$

and the coefficients n, m and k are expressed as:

$$n = \frac{\partial \ln(\mu)}{\partial \ln(T_L)}, \ m = \frac{\partial \ln(\lambda)}{\partial \ln(T_L)}, \ k = \frac{\partial \ln(\rho)}{\partial \ln(T_L)} \tag{1.39}$$

where μ, λ and ρ denote the viscosity, the thermal conductivity and the density of the fluid respectively.

Fig. 10 shows the evolution of those coefficients as a function of both pressure and temperature for Freon R134A as a coolant fluid.

Since the Nusselt number Nu_w varies linerly with the square root of the Reynolds number Re_w(see Fig. 11), the expressions for the sensitivity coefficients F and G and can be simplified :

$$F = 0.5A_w \tag{1.40}$$

and

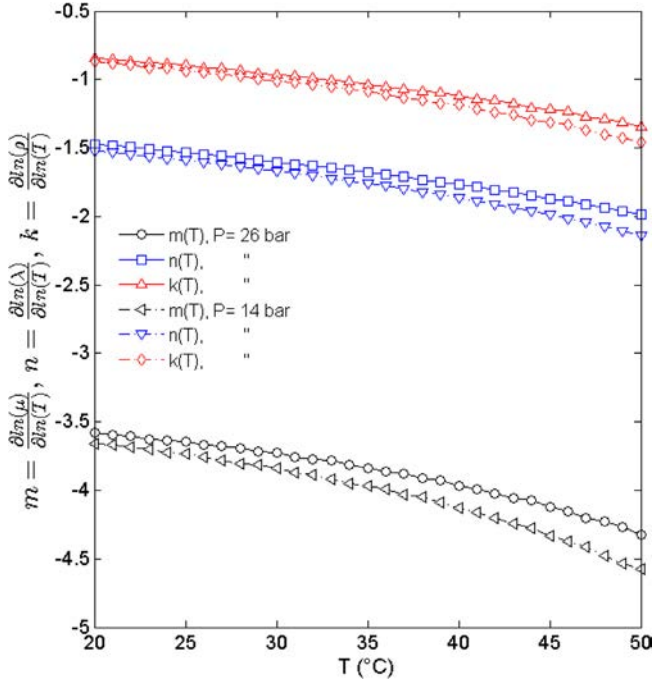$$G = -\alpha_0 T_w + A_w\left(1 + n - \frac{m}{2} + \frac{k}{2}\right) \tag{1.41}$$

9

Fig. 10. Variation of the n, m, and k coefficients (equation) with the fluid temperature for two pressures (14 and 26 bar).
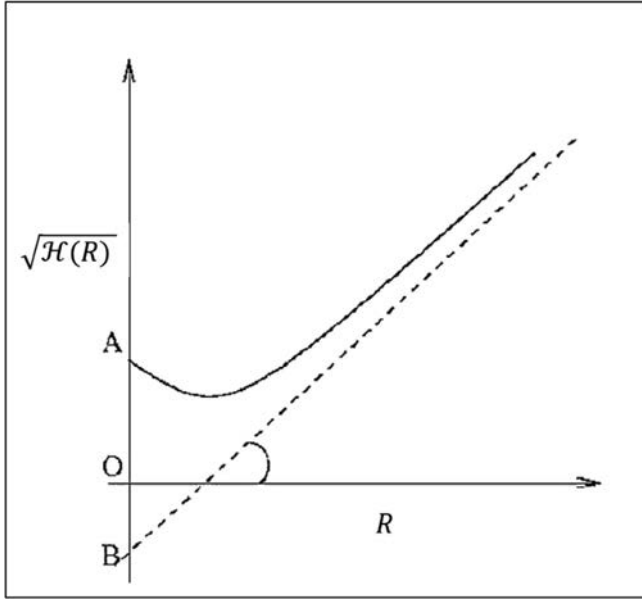

Fig. 11. Schematic diagram of the graphical resolution method for the fluctuation diagram.

Therefore, the sensitivity coefficients mainly depend on the fluid temperature T_w, the sensor's overheat ratio a_w and the physical properties of the fluid. For low values of the overheat coefficient a_w (which means that the sensor is operated in "cold wire" mode), the coefficient F decreases and the measurement is only sensitive to the fluid temperature fluctuations t'. On the contrary, for greater values of the the overheat ratio (which means that the sensor is operated in "hot wire" mode), the coefficient F increases and the measurement become more sensitive to velocity fluctuations u'.

By squaring Eq. (1.33), we finally obtain the following relation also called the variance equation of the fluctuation diagram:

$$\frac{e_w^{'2}}{e_w^2} = F^2\left(\frac{u^{'2}}{U_L^2}\right) + 2FG\left(\frac{u't'}{U_L T_L}\right) + G^2\left(\frac{t^{'2}}{T_L^2}\right) \tag{1.42}$$

It is possible to deduce from equation (1.42) the fundamental equation of the so-called fluctuations diagram by time-averaging equation and dividing by G^2:

$$\sqrt{\mathscr{H}(\mathscr{R})} = \frac{\sqrt{\overline{e_w^{'2}}}}{\overline{e_w}G} = \left[\mathscr{R}^2\left(\frac{\overline{u^{'2}}}{\overline{U_L^2}}\right) + 2\mathscr{R}\frac{\sqrt{\overline{u^{'2}}}}{\overline{U_L}}\frac{\sqrt{\overline{t^{'2}}}}{\overline{T_L}}\mathscr{R}_{U,T} + \left(\frac{\overline{t^{'2}}}{\overline{T_L^2}}\right)\right]^{0.5} \tag{1.43}$$

where $\mathscr{R}_{U,T}$ and $\mathscr{R}$ are defined respectively as:

$$\mathscr{R}_{U,T} \triangleq \frac{\overline{u't'}}{\sqrt{(\overline{u^{'2}}\overline{t^{'2}})}} \tag{1.44}$$

And

$$\mathscr{R} \triangleq -\frac{F}{G} \tag{1.45}$$

Which only depends, for given flow thermal hydraulic conditions, on the sensor overheat ratio a_W.

Equation (1.43) is a parabolic equation whose a schematic graphical representation is given on Fig. 11.

The experimental procedure then consists of varying the coefficient R by injecting several currents into the sensor (which leads to a change of the overheat ratio a_W) to obtain the experimental curve $\mathscr{H}(\mathscr{R})$. From a practical point of view, fifteen values of the overheat ration a_W are needed to get an accurate fluctuations diagram. Then, using a least squares regression method, we can determine the fitting coefficients of the parabola (equation and deduce the equation (1.43) variances of the velocity and temperature fluctuations $u^{'2}$ and $t^{'2}$ as well as their correlation $\overline{u't'}$ using Eqs. (1.43) and (1.44). It can be noticed that the temperature fluctuations $t^{'2}$ is given by the intercept of the diagram and that the velocity fluctuations are given by the slope of the asymptote. As a result, the measurement accuracy of the temperature fluctuations is greatly affected by the signal-to-noise ratio of the hot wire at low overheating whereas the accuracy of the velocity fluctuations measurements depends on a correct determination of the asymptotic slope which requires to operate at high overheat ratios. Unfortunately, boiling occurrence on the sensor may limit the highest value of the overheat ratio.

3.2.5.1. Frequency compensation procedure. As already mentioned, the bandwidth of a constant current anemometer is limited by the thermal inertia of the sensor. This can be an important source of errors while determining the fluctuating quantities using the fluctuation diagram method. Indeed, high frequencies may be filtered by the anemometer, which may lead to a significant underestimation of the voltage signal variance $e_w^{'2}$. To overcome this limitation, we propose to use a signal processing procedure which makes it possible to compensate a posteriori for the sensor filtering effect (Wroblewski and Eibeck (1991), Tagawa et al. (1998), Lemay et al. (2003), Arwatz et al. (2013), Khine et al. (2013)). The frequency compensation procedure consists in applying to the experimentally measured voltage signal (which is attenuated by the filtering effect of the sensor) an amplifying filter whose cutoff frequency is equal to the theoretical cutoff frequency of the anemometer f_C but whose gain is opposite. This procedure is described on Fig. 12. In order to achieve this compensation, four steps are necessary:

- First, the experimental voltage signal is filtered using a digital low-pass filter in order to eliminate the electronic noise measurement and prevent it from being amplified during the procedure. The cutoff frequency is chosen equal to 10*KHz*,
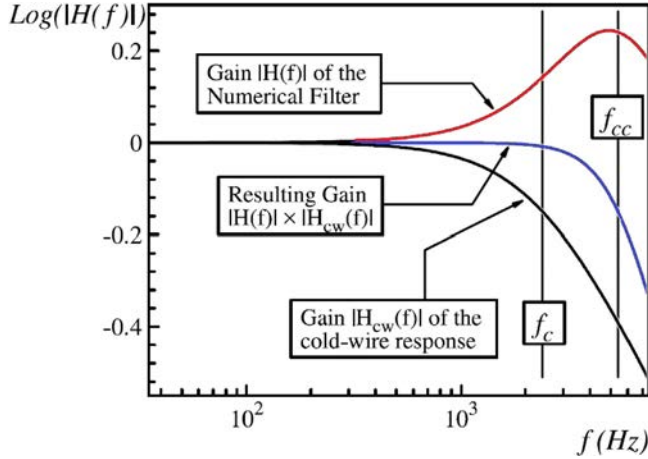
Fig. 12. Schematic diagram of the digital frequency compensation procedure (from Lemay et al. (2003)).

- The signal is then transposed into the frequency domain using the Fourier transform,
- The signal is then compensated by multiplying each of its frequency component by $1 + if/f_C$.
- Finally, the temporal compensated signal is then obtained by applying the inverse Fourier.

The use of this procedure requires to know the anemometer cutoff frequency f_C. According to Comte-Bellot (1976), it can be expressed as:

$$f_c \triangleq \frac{1}{2\pi\tau_w} = \frac{2Nu_{w,f}\lambda_f}{\pi d^2 C_{pw}\rho_w(1+a_w)} \qquad (1.46)$$

This value depends on both the flow conditions (Nusselt number Nu_w) and the sensor overheat ratio a_w.

3.2.5.2. Maximum achievable temperature on the the probe surface. When the temperature over the sensor surface is high enough, boiling may occur. It is no longer possible to use the previous methodology which assumes a convective heat transfer between the proble and the surrounding flow. It is then important to estimate as accurately as possible the conditions leading to boiling occurrence. Some tests have been performed. The results are shown on Fig. 13 where the heat flux has been plotted against the wire temperature T_w which can be deduced from the electrical resistance of the wire R_w. Two different behaviors can be observed. First, the heat flux varies linearly with the wire overheating, which corresponds to a convective single phase heat transfer exchange (points $1 \rightarrow 2$). For higher values of the heat flux, a slope break is observed, which corresponds to the occurence of nucleate boiling (point 2). We can observe that the slope of the curve is higher than for the first regime which confirms an increase of the heat transfer coefficient in boiling conditions compared to single phase heat transfer. If the heat flux still increases, the curve flattens and tends to approach the boiling crisis (which is not represented on this plot). As the heat flux is imposed, when boiling crisis occurs, the temperature of the wire suddenly increases and can reach the melting temperature of the sensor unless the electric power is cut off. According to the range of thermal hydraulic parameters considered in our work, nucleate boiling occurs for when the temperature of the wire is eight to thirteen degrees higher than the saturation temperature.

Those superheats have been validated using the model of Hsu (1962). This model provides with a relation between the wall superheat which is required for boiling and the size of the active nucleation sites. The model assumes that vapor bubbles are created within a thermal boundary layer and then detach the wall since they have reached a critical size. After the detachment of the bubble, some cold liquid
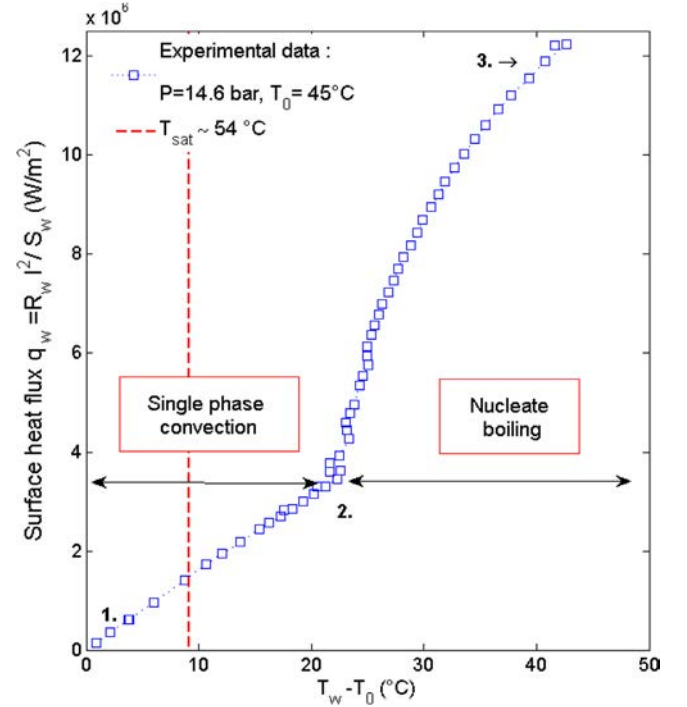

Fig. 13. Experimental boiling curve obtained for a wire probe in diameter (Ps = 14 bar, U = 2 m/s, Ts = 45 °C, Xeq,s = 0.34 diameter of the probe d = 5 μm).

rewets the wall and the thermal boundary layer is reformed by unsteady conduction. Assuming that the steam embryo grows up if the temperature of the top of the bubble is greater than the temperature required to maintain its equilibrium, it is possible to define the critical sizes (minimum and maximum) of a cavities allowing a trapped embryo to grow up. Hsu (1962) assumes that the radius of a vapor embryo, denoted R_e, is related to the cavity radius R_C by the following relation:

$$\begin{bmatrix} R_{c,max} \\ R_{c,min} \end{bmatrix} = \frac{\delta_t}{4}\left(1 - \frac{\Delta T_{sat}}{\Delta T_w}\begin{bmatrix} + \\ - \end{bmatrix}\sqrt{\left(1 - \frac{\Delta T_{sat}}{\Delta T_w}\right)^2 - \frac{12.8\sigma T_{sat}}{\rho_g h_{fg}\delta_t \Delta T_w}}\right) \qquad (1.47)$$

where ΔT_{sat}, ΔT_w are defined as below:

$$\Delta T_{sat} = T_{sat} - T_0 \qquad (1.48)$$

$$\Delta T_w = T_w - T_0 \qquad (1.49)$$

And δ_t which is the thickness of the thermal boundary layer is given as:

$$\delta_t \frac{\lambda_f}{h} \frac{d}{Nu_{w,f}} \qquad (1.50)$$

According to Eq. (1.47), if the radius of the cavity is too large ($R_c > R_{c,max}$), the steam embryo is too large and its top will be located outside from the thermal boundary layer. As a consequence, the vapor embryo will condense, thus preventing its growth. On the contrary, if the cavity radius is too low ($R_c < R_{c,min}$), the steam embryo is too small and the liquid temperature in the boundary layer not high enough to allow the vapor nucleus to grow.

Fig. 14 shows the results obtained using the model of Hsu (1962) for a Tungsten wire with a diameter equal to 5 μm for the following thermal hydraulic conditions: $P_s = 14$ bar, $U_L = 2$ m/s, $T_0 = 20$ °C and $T_0 = 45$ °C. The Nusselt number (Eq. (1.50)) are calculated using the correlation of Kramers (1946) (see Eq. (1.13)).

The minimum superheat required for the onset of nucleate boiling corresponds to the top of the curves shown in Fig. 18. According to Hsu's model, the superheats are between 8 and 15 °C, which
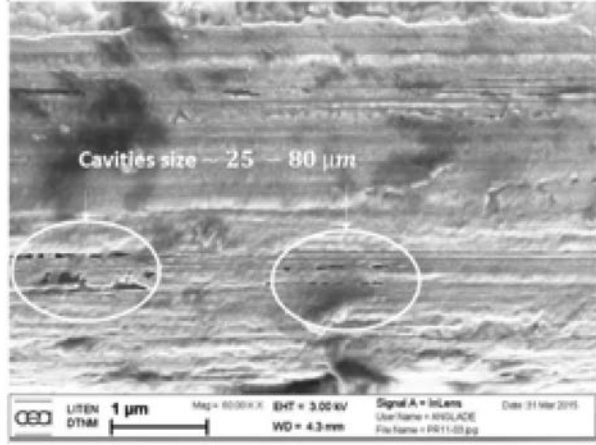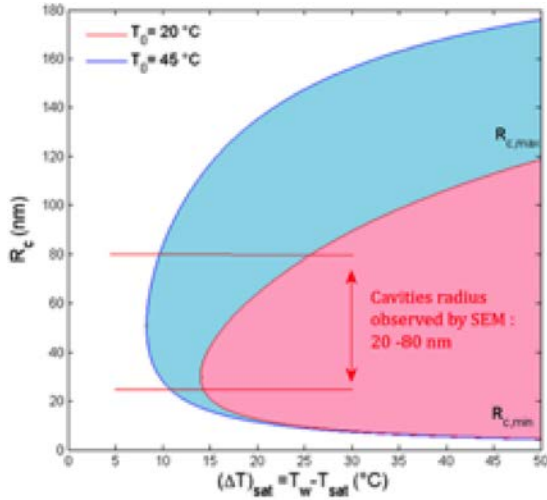
Fig. 14. (Left) Influence of the cavities size on the difference between the wire temperature required for the onset of boiling (Tw) and the saturation temperature Tsat, according to the model of Hsu (1962) (P = 14 bar, UL = 2 m/s). The colored areas correspond to the zones where the cavities are activated by the superheating ΔTsat = Tw-Tsat - (right) Surface condition of a new Tungsten probe d = 5 μm. The image is obtained using a scanning electron microscope (SEM).
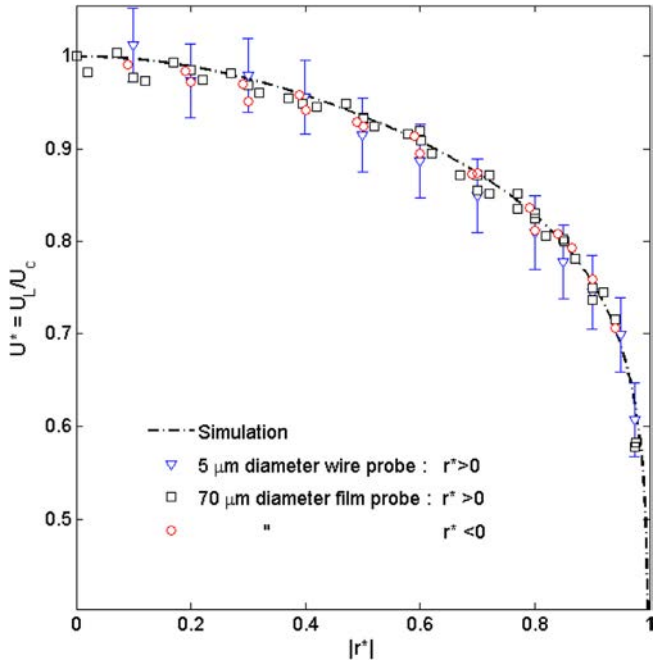
Fig. 15. Run G3Q0: Non dimensional liquid velocity profile obtained with both probes and comparison with the model of Deissler (1951).

corresponds to cavities with a radius btween 30 and 40 nm. Those values are consistent with the characteristic sizes of cavities measured using a scanning electron microscope as shown in Fig. 18.

4. Experimental results

4.1. Mean liquid velocity and temperature

As specified in section 2, the DEBORA test section is a tube whose inner diameter is 19.2 mm. The heated length is 3.5 m. Local measurements (liquid temperature, liquid velocity) were performed in the exit cross section using a hot wire and a hot film probe whose characteric sizes are reminded below:

- A hot wire probe $d = 5\mu m$ and $l = 1.25mm$
- A hot film probe $d = 70\mu m$ and $l = 1.25mm$

Table 5
Experimental conditions of the R134A DEBORA data base (isothermal and heated single phase flows).

Run	P (bar)	G (kg m^{-2} s^{-1})	T_{in} (°C)	q_p (kW m^{-2})	T_{out} (°C)	$x_{eq,\ out}$
G3Q0	13.9	2993	20.0	0	20.0	−0.297
G3Q20	13.9	2998	20.0	21.0	23.4	−0.283
G3Q40	13.9	2995	20.1	39.4	26.6	−0.253
G3Q60	13.9	2999	20.0	59.9	29.9	−0.222
G3Q80	13.9	3000	20.1	81	33.7	−0.186
G1Q20	13.9	1011	20.1	19.7	30.1	−0.221
G2Q20	13.9	1998	20.0	19.6	25.0	−0.269
G3Q20	13.9	2998	20.0	21.0	23.4	−0.283

The probe was held and positioned along the radial direction using a traversing system. Data points were taken at 13 radial positions over one-half diameter.

Table 5 summarizes the flow conditions corresponding to isothermal and heated single phase flows. Eight runs have been performed.

The exit equilibrium quality is defined as:

$$x_{eq,out} \triangleq \frac{h_{l,out} - h_f}{h_{fg}} \tag{1.51}$$

where $h_{l,out}$ is the liquid enthalpy at the exit of the test section.

According to section 3, for such a pressure, the maximum achievable temperature for the probe is equal to 62 °C. That corresponds to an overheat ratio a_w ranging from 0.14 to 0.2 depending on the run.

Fig. 15 shows the non-dimensional liquid velocity profile U_L^* (defined as the ratio between the liquid velocity U_L and the velocity on the centerline of the tube U_C) as a function of the non-dimensional radial position r^* (defined as the ratio between the radial position r and the radius of the pipe R) for run G3Q0. We also have plotted on the same figure the theoretical liquid velocity profile obtained using the model of Deissler (1963). First, this plot confirms that the flow is axisymmetric. Despite the probe being located near the exit of the heated tube, there is no influence from the geometry of the region. It also shows that whatever the probe, the measured liquid velocity profiles are consistent with each other even in the region of inner wall. In our experiments, the nearest measurement position is located at 0.3 mm from the wall. Finally, we can also notice that there is a good agreement between the experimental results and the theoretical profile.

In order to describe more in detail the liquid velocity field in the region close to the wall, Fig. 16 plot the results of run G3Q0 with respect to wall units y$^+$ and U_L^+ which are defined as, respectively:
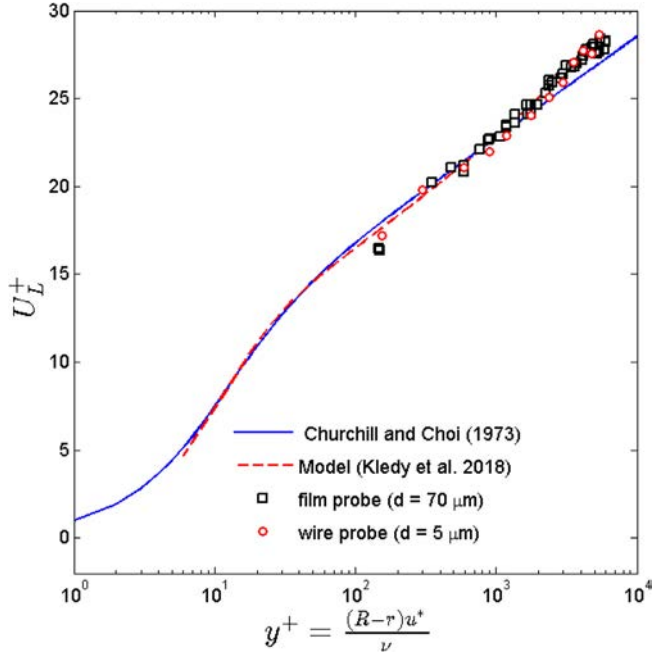
Fig. 16. Run G3Q0 Non dimensional liquid velocity profile U_L^+ as a function of the non dimensional radial coordinate. y^+

$$y^+ \triangleq \frac{(R-r)u^*}{\nu_L} \tag{1.52}$$

and

$$U_L^+ \triangleq \frac{U_L}{u^*} \tag{1.53}$$

where ν_L is the kinematic viscosity of the liquid and where the friction velocity u^* is defined as:

$$u^* = \sqrt{\frac{\tau_w}{\rho_L}} \tag{1.54}$$

As the wall shear stress τ_w is not measured, it has been calculated using the friction correlation of MacAdams (1954):

$$\tau_w = \frac{C_f}{2} \frac{G^2}{\rho_L} \tag{1.55}$$

where C_f is the friction coefficient:

$$C_f = 0.036 Re^{-0.182} \tag{1.56}$$

Re is the Reynolds number defined as :

$$Re = \frac{GD}{\mu_L} \tag{1.57}$$

The physical properties of the liquid are calculated at the exit liquid temperature T_{out}. The range of validity of the correlation of MacAdams is $4.\,10^4 < Re < 10^7$.

We also plot on Fig. 16 the liquid velocity profile calculated by the model of Deissler (1963) and the model of Churchill and Choi (1973). This model provides with a single expression for the velocity profile whatever the distance from the wall.

$$U_L^+ = y^+ \left[1 + \left(\frac{y^+}{9.025\ln(y^+)} \right)^2 \right]^{-0.5} \tag{1.58}$$

As already mentioned, there is a good agreement between experimental results and the predictions given by theoretical models. However, we can observe that the hot film probe tends to underestimate the liquid velocity (compared to theoretical models) in the vicinity of the wall whereas the hot wire still agrees with both models.
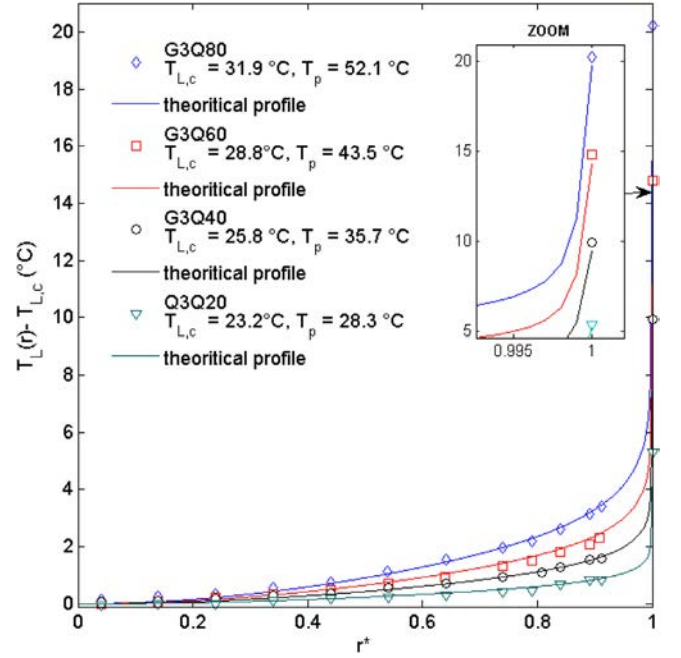

Fig. 17. Influence of the heat flux on the liquid temperature profiles $G = 3000$ kg.m^{-2}.s^{-1}.

This behaviour clearly reflects the effect of intrusivity of the hot-film probe coming from its larger diameter.

Mass balance have also been checked for all the tests from Table 5. As mentionned before, the nearest measurement position is located at 0.3 mm from the wall. Consequently, and to a first approximation, we may assume that the liquid velocity profile linearly connects to zero at the wall. Under such assumption, the maximum observed discrepancy between the imposed mass flow rate and the one deduced from the experimental data is 3%.

Figs. 17–20 represent the liquid velocity and temperature profiles for non isothermal runs given in Table 5. Liquid velocity profiles are plotted in terms of dimensionless velocity ($U_L^* = U_L/U_C$ where U_C is the
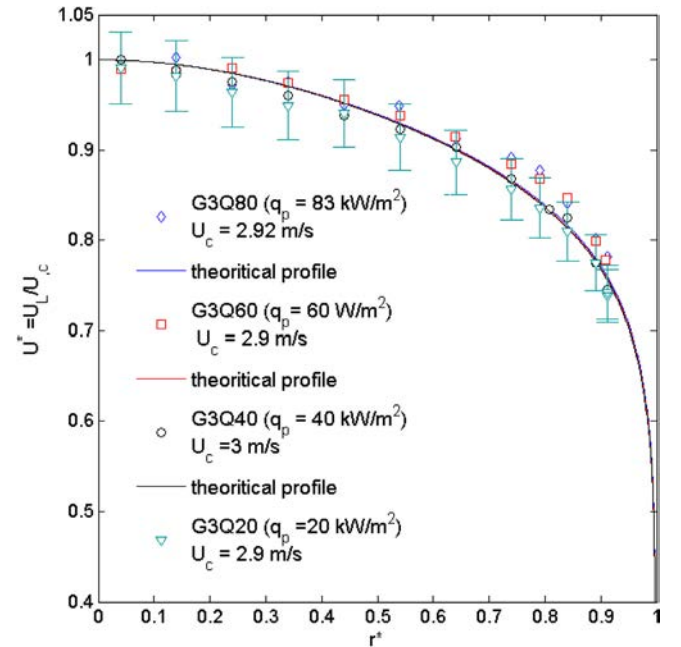

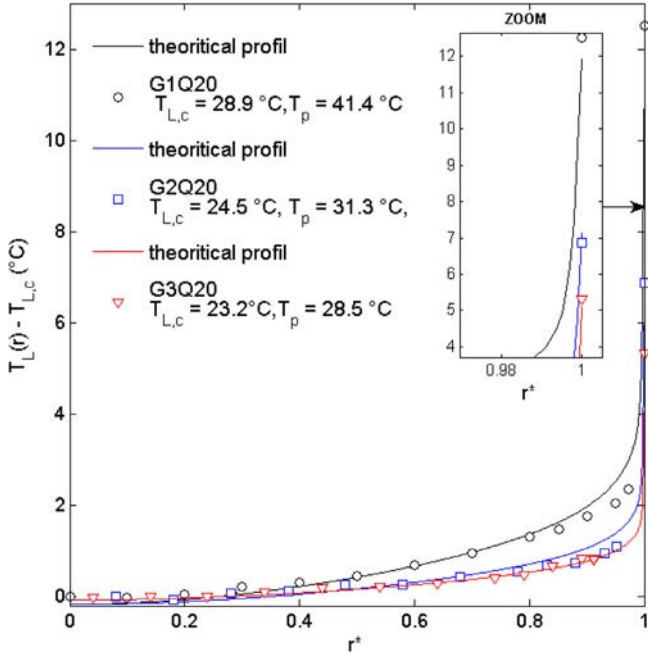**Fig. 18.** Influence of the heat flux on the liquid velocity profile $G = 3000$ kg.m^{-2}.s^{-1}.

Fig. 19. Influence of the mass flux on the liquid temperature profile. $q_p = 20kW \cdot m^{-2}$

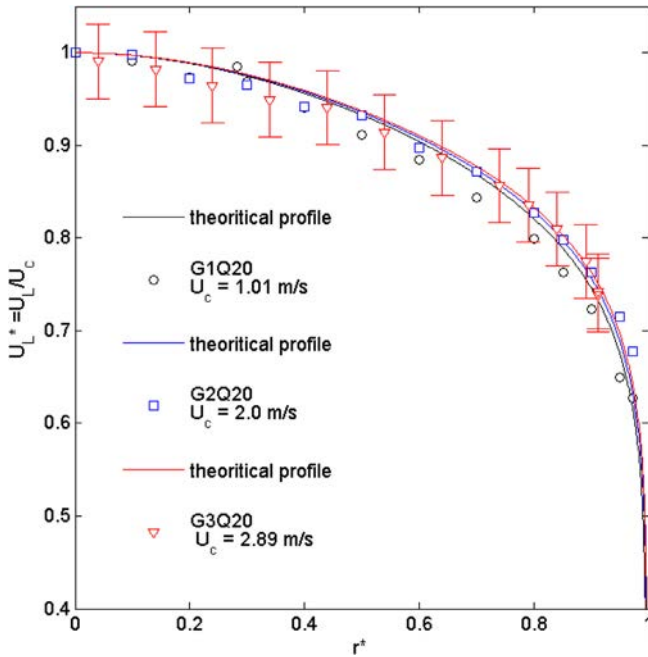**Fig. 20.** Influence of the mass flux on the liquid velocity profile. $q_p = 20kW \cdot m^{-2}$

liquid velocity on the centerline of the tube) whereas the temperature profiles are represented in terms of temperature differences between the local liquid temperature and the temperature measured on the axis of the tube $T_L - T_{L,C}$. We also plotted on those figures the temperature of the heated wall, which is measured using the Platinum sensors described in Section 2 The liquid velocity profile is calculated using the model of Deissler (1963) and the temperature profile is deduced from the liquid one using the analogy of Prandtl (Todreas and Kazimi, 1990).

For all the runs, there is a good agreement between the experimental and the theoretical results up to the radial position $r^* = 0,95$ which corresponds to distance from the wall equal to 480 μm. The maximum relative deviation between experimental data and numerical

one is 4% for the liquid velocity profile whereas the maximum deviation for the liquid temperature is 0.2 ℃. We can also notice that the measured wall temperatures are consistent with the temperatures predicted using the model of Deissler (1963) coupled with the Prandtl analogy. The maximum deviation is 0.5 ℃ which is consistent with the uncertainty of the wall temperature measurement.

Energy balance have also been checked for non isothermal tests from Table 5. As presented before, the liquid temperature profiles were assumed to linearly connect to the measured wall temperature. The maximum observed discrepancy between the measured liquid temperature at the exit of the test section and the temperature calculated by energy balance is 0.2 ℃ which is consistent with the uncertainty of temperature measurements given in Table 3.

If the liquid temperature profiles seem to be influenced by the heat flux (for an imposed mass flux, they flatten when the heat flux decreases as shown on Fig. 17), the impact is weaker on the velocity profiles. This means that the liquid temperature gradient is too small to significantly affect the liquid density and as a consequence the velocity profiles due to boyancy effects. In order to describe more accurately the liquid temperature and velocity behaviour in the vicinity of the wall, we have plotted on Fig. 21 the results of the previous runs with respect to wall units y^+, U_L^+ and T_L^+ where T_L^+ is defined as:

$$T_L^+ \triangleq \frac{T_P - T_L}{t^*} \tag{1.59}$$

And t^* is defined as:

$$t^* \triangleq \frac{q_p}{\rho_L C_{PL} u^*} \tag{1.60}$$

We observe that the temperature profiles T_L^+ all superimposed on the same curve which seems to linearly evolve with the logarithm of the distance to the wall y^+. A similar trend can be noticed observed for the liquid velocity profiles U_L^+. We can also see that the slopes of the curves on Fig. 25 are very similar for the temperature and the velocity, which confirms the validity of the Prandtl analogy.

4.2. Turbulent fluctuations measurements

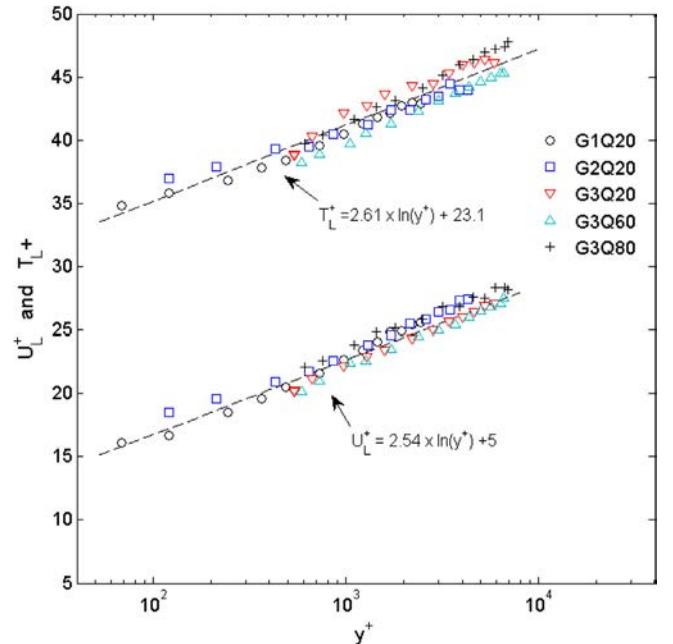In this section, we give some detailed information about the

Fig. 21. Evolution of the velocity U_L^+ and the temperature T_L^+ as a function of the wall distance y^+ for non-isothermal tests from Table 5.
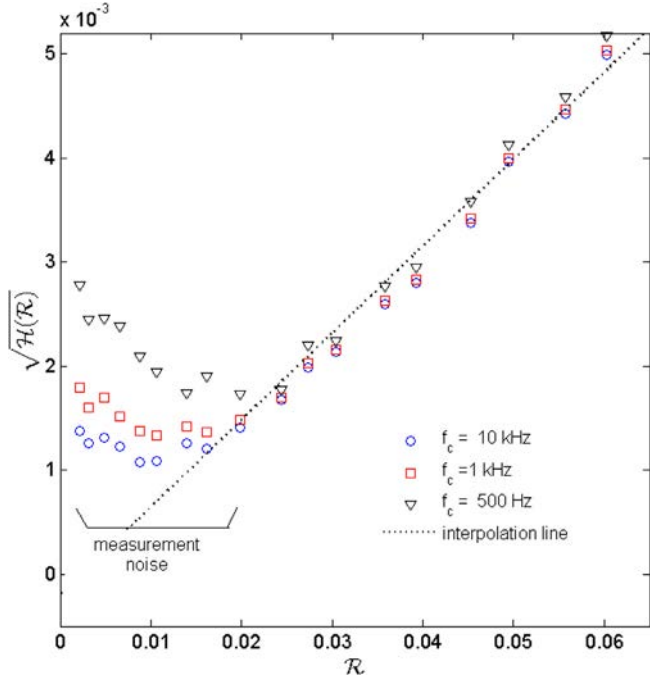
14

Fig. 22. Run G1Q0 - Fluctuation diagram for different compensation frequencies.$r^* = 0.9$
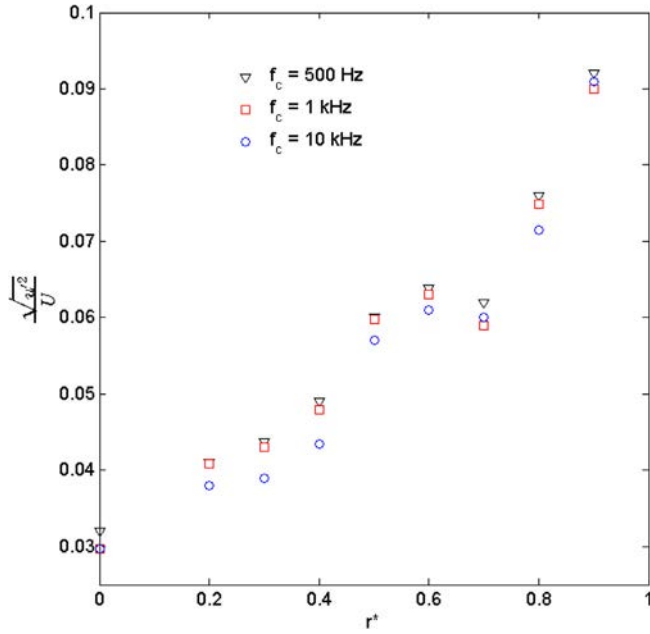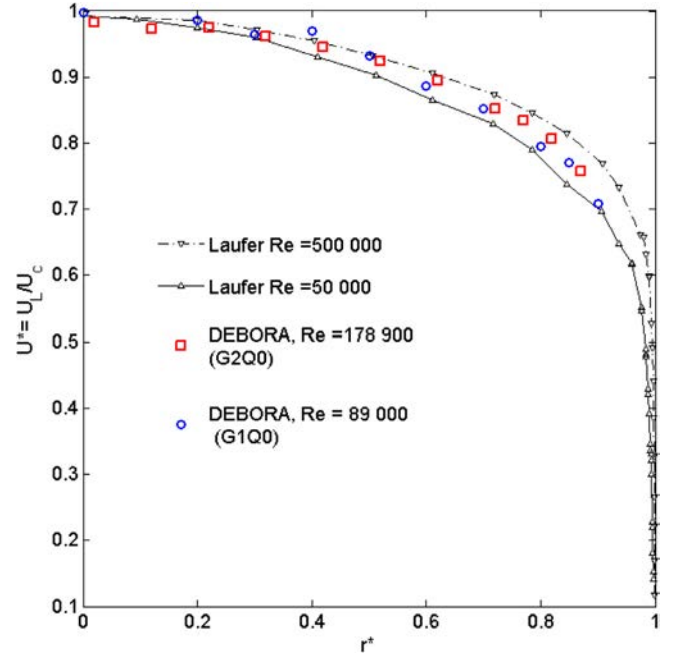

Fig. 24. Comparison between the experimental data from DEBORA Run G1Q0 and run G3Q0 with data from Laufer (1954). Non dimensional liquid velocity profiles.
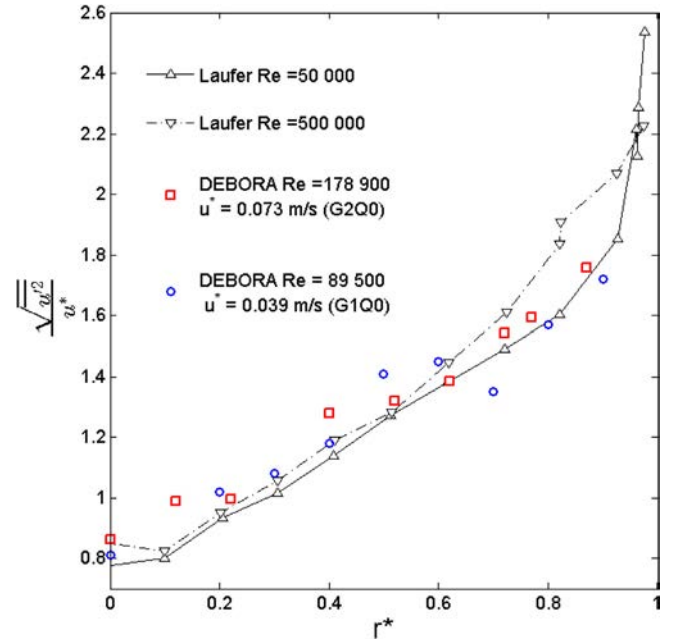

Fig. 23. Turbulent velocity fluctuations $\sqrt{\overline{u'^2}}$ obtained for test G1Q0 - Three different values of the cutoff frequency have been used.

Fig. 25. Comparison between the experimental data from DEBORA Run G1Q0 and run G3Q0 with data from Laufer (1954). Normalized liquid velocity fluctuations.

turbulent structure of the flows. It is possible to measure the turbulent liquid velocity fluctuations $\sqrt{\overline{u'^2}(r)}$ using the fluctuation diagram method described is the present paper.

Two tests were performed. The boundary conditions of thoses tests are described in Table 6.

Those two runs are adiabatic and were carried out at a pressure of 26 bar ($T_{sat} = 79^\circ C$) in order to get the maximum achievable temperature of the sensor without triggering nucleate boiling on its surface, which corresponds to a temperature equal to 82 °C and an overheat ratio a_w equal to 0.21. Hot wires probes (diameter $d = 2.5\mu m$) were used because of their smaller sizes compared to hot film probes.

Table 6
Boundary conditions for the liquid velocity fluctuations tests.

Run	P (bar)	G (kg m^{-2} ms^{-1})	T$_{in}$ (°C)	q$_p$ (kW m^{-2})	T$_{out}$ (°C)	x$_{eq, out}$
G1Q0	26	1000	19.9	0	19.9	− 0.87
G3Q0	26	2998	19.9	0	19.9	− 0.81

To get accurate measurements of turbulent fluctuations, it is necessary to compensate the raw signal using the procedure described in the paper. According to Eq. (1.46), it is theoretically possible to

determine the cutoff frequency. For run G1Q0, we calculate a theoretical cutoff frequency equal to 10 kHz for an overheat ratio $a_w = 0.21$, the Nusselt number being determined using the correlation of Kramers (1946). As the cutoff frequency may be influenced by many parameters like probe fouling, we characterized the impact of this frequency on the determination of the turbulent quantities.

For adiabatic flows, the turbulent temperature fluctuation should be null and the theoretical expression of the fluctuation diagram (Eq. (1.43)) reduces to the following linear expression:

$$\sqrt{\mathscr{H}(\mathscr{R})} = \frac{\sqrt{\overline{e_w'^2}}}{e_w G} = \mathscr{R}(a_w) \times \frac{\sqrt{\overline{u'^2}}}{U} \tag{1.61}$$

Where turbulent velocity fluctuations can then be derived from the slope determination of this curve.

For $\mathscr{R} > 0.02$, we can observe on Fig. 22 a linear behaviour as expected. In addition, we can also notice that the slope seems to be weakly affected by the cutoff frequency. This indicates for these tests, most of energy is at large scales, *i.e.* low frequencies in energy spectra.

On the other hand, for low values of $\mathscr{R}$, the experimental data deviate from the linear behaviour, which can be explained by a low signal-to-noise ratio, as the tests are adiabatic (no temperature fluctuations).

This behaviour clearly indicates that it is not posssible to measure the fluctuations of the liquid temperature unless the signal-to-noise ratio is increased at low overheat.

The turbulent liquid velocity fluctuations $\sqrt{\overline{u'^2}}(r)$ have been plotted on Fig. 23 for several radial positions r^*, using different cutoff frequencies for compensating the hot-wire response ($f_c = 500\ Hz$, $f_c = 1\ KHz$ and $f_c = 10\ KHz$). It can be seen that this frequency has very little impact on the obtained results whatever the radial location of the measurement (Fig. 24).

Those results have also been compared with reference data from the literature such as those of Laufer (1954). The experimental data from Laufer (1954) were obtained in a turbulent flow established in a wind tunnel (diameter $D = 0.254m$). The measurements were carried out using a hot wire ($d = 2.5\mu m - l = 600\mu m$) for two different Reynolds numbers ($Re = 5.\ 10^4$ and $Re = 5.\ 10^5$) which frame our test conditions. ($Re = 89.\ 10^3$ and $Re = 178.\ 10^3$) where the Reynolds number is defined by Eq. (1.57).

In order to compare our experimental results with those of Laufer (1954), liquid velocity fluctuations were normalized using the friction velocity u^* given by Eqs. (1.54) to (.57)).

There is a good agreement between our experimental results and the data from Laufer (1954) from both the point of view of average and turbulent quantities. As a result, we can now consider that the database obtained by anemometry is validated for the mean liquid velocity and temperature profiles but also for the velocity fluctuations.

5. Conclusions

The work presented in this paper focuses on the development of anemometry in single phase flow with heat addition. It is the first part of an overall study which aims to develop an experimental technic for measuring the liquid velocity in boiling flows for operating conditions that reproduce the ones encountered within a PWR. Due to the difficulties in performing local measurements for high pressure and high temperatures conditions, this work was performed with a simulating fluid (Freon R134a) following well-established scaling criteria for boiling crisis.

The Freon R134a being an electrical insulator, it has been possible to use Tungsten wire probes whose diameter can be as small as $d = 2.5\mu m$ instead of hot film probes whose diameter are larger. Those wires have been coated with a thin layer of Saphhire in order to prevent any chemical alteration by the Fluorine which is present in Freon R134a.

The method of multiple overheats has been used to determine both the mean liquid velocity and temperature using a single sensor. To take into account for temperature effects, an original approach based on a new non-dimensional representation of the calibration curve has been proposed. This new representation reduces the calibration curve to a very convenient linear fit whatever the liquid temperature. Using the multiple overheats method, it is also possible to characterize the turbulent fluctuations of the flow using the fluctuation diagram method. To get an accurate determination of the fluctuating quantities, it is necessary to compensate the thermal inertia of the wire, which has been done numerically and to reach a high overheat ratio on the sensor. However, the maximum achievable temperature at the surface of the sensor is limited by the occurrence of boiling. The observed boiling temperature is consistent with the surface conditions and especially the size of the active nucleation sites.

Some tests have been performed for isothermal and non isothermal flow conditions. The mean liquid and temperature profiles have been measured for several conditions using hot wires and hot films probes. Results are consistent with theoretical profiles even in the vicinity of the wall, the nearest measurement position being located at 0.3 mm from the wall.

In addition, the velocity fluctuations have also been measured using the fluctuation diagram method. Liquid velocity fluctuations are consistent with the ones obtained by Laufer (1954) in a range of Reynolds number that framed our experimental conditions. Liquid temperature fluctuations were not measured because the signal-to-noise ratio was too bad for sensor's low overheats.

The next work will now consist on using this technic for boiling two-phase flows.

Declaration of Competing Interest

The authors declare that they have no known competing financial interests or personal relationships that could have appeared to influence the work reported in this paper.

References

Arwatz, G., Bahri, C., Smits, A.J., Hultmark, M., 2013. Dynamic calibration and modeling of a cold wire for temperature measurement. Meas. Sci. Technol. 24.

Barre, S., Dupont, P., Dussauge, J.P., 1992. *Hot-wire measurements in turbulent transonic flows*. Eur. J. Mechan. 11 (3).

Barre, S., Quine, C., Dussauge, J.P., 1994. Compressibility effects on the structure of supersonic mixing layers: Experimental results. J. Fluid Mech. 259, 47–78.

Bestion, D., Gaviglio, J., Bonnet, J.P., 1983. Comparison between constant-current and constant-temperature hot-wire anemometers in high-speed flows. Rev. Scient. Instrum. 54 (11), 1513–1524.

Bonnet, J.P., Knani, M.A., 1988. Calibration and use of inclined hot wires in a supersonic turbulent wake. Exp. Fluids 6 (3), 179–188.

Bruun, H.H., 1995. Hot-Wire Anemometry : Principles and signal. Oxford University Press Inc., New-York.

Bruun, H.H., 1996. Hot film anemometry in liquid flows. Meas. Sci. Technol. 7.

Churchill, S.W., Choi, B., 1973. Theoretically based correlating equations for the local characteristics of fully turbulent flow in smooth pipes. AiCHE 19, 196–197.

Comte-Bellot, G., 1976. Hot wire anemometry. Annu. Rev. Fluid Mech. 8, 209–231.

Corrsin, S., 1947. Extended applications to the hot-wire anemometer. Rev. Sci. Instrum. 18.

Deissler, R.G., 1963. Turbulent heat transfer and temperature fluctuations with uniform velocity and temperature gradients. Int. J. Heat Mass Transfer 6.

Dix G., 1971, Vapor void fractions for forced convection with subcooled boiling at low flow rates, Ph. D. Thesis, University of California.

Francois, F., Delhaye, J.M., Clement, Ph., 2011. The distribution parameter in the drift flux modeling of forced convective boiling flows. Multiph. Sci. Technol. 23 (1), 77–100.

Garnier, J., Manon, E., Cubizolles, G., 2001. Local measurements on flow boiling of refrigerant 12 in a vertical tube. Multiph. Sci. Technol. 13 (1), 1–111.

Guelfi A., Boucker M., Hérard J.M., Péturaud P., Bestion D., Boudier P., Fillon P., Grandotto M., Hervieu E., 2005, A new multiscale platform for advanced nuclear thermal-hydraulics, status and prospect of the NEPTUNE project, NURETH 11, Avignon.

Hasan, A., Roy, R.P., Kalra, S.P., 1992. Velocity and temperature fields in turbulent liquid flow through a vertical concentric annular channel. Int. J. Heat Mass Transf. 35, 1455–1467.

Hösler E.R., Flow patterns at two-phase high pressure (steam-water) flow with heat addition, AIChE Symposium Series, 64, (82), pp. 54–66.

Hsu, Y.Y., 1962. *On the size range of activating nucleate cavities on a heating surface*, Journal of. Heat Mass Transf. 84.

Inoue, A., Kurosu, T., Aoki, T., Mitsutake, T., Morooka, S., 1995. Void fraction distribution in BWR fuel assembly and evaluation of subchannel code. J. Nucl. Sci. Technol. 32 (7), 629–640.

Khine, S.M., Houra, T., Tagawa, M., 2013. An adaptative technical compensation for the constant-current hot-wire anemometers. Open J. Fluid Dynam. 3, 95–108.

Klédy M., 2018, Développement d'une méthode de mesure du champ de vbitesse et de température liquide en écoulement diphasique bouillant en conditions réacteurs ou simulantes, Ph. D. Université de Grenoble (in French).

Kovasznay, L.S.G., 1953. Turbulence in supersonic flow. J. Aeron. Sci. 20, 657–682.

Kramers, H., 1946. Heat transfer from spheres to flowing media. Physica 12.

Lee, T.H., Park, G.C., Lee, D.J., 2002. Local flow characteristics of subcooled boiling flow in a vertical concentric annulus. Int. J. Multiph. Flow 28, 1361–1368.

Lemay, J.L., Benaissa, A., Antonia, R.A., 2003. Correction of cold-wire response for mean temperature dissipation rate measurements. Exp. Therm Fluid Sci. 27.

Lemonnier, H., Julien, P., 2011. On the use of nuclear magnetic resonace to characterize vertical two-phase bubbly flows. Nucl. Eng. Des. 241 (3), 978–998.

Laufer, J., 1954. The structure of turbulence in fully developed pipe flow, Tech. rept.

NACA-TN-2954, NACA-TR-1174. Nat. Advis. Comm. Aero.

MacAdams, W.H., 1954. Heat Transmission. Mc Graw-Hill.

Morkovin M.V., 1956, Fluctuations and hot-wire anemometry in compressible flows, Report from Advisory Group for Aerospace Research and Development (North Atlantic Treaty Organization).

Ndoye M., 2008, Anémométrie fil chaud à température variable : application à l'étude d'une couche de mélange anisotherme, Ph. D. Université de Poitiers (in French).

Perez, C.E., Hassan, Y., 2010. PTV experiments of subcooled boiling flow through a vertical rectangular channel. Int. J. Multiph. Flow 36, 691–706.

Resch F., Coantic M., 1969, Study on the hot wire and the hot film in the water, White Coal, 2, 1969.

Roy, R.P., Velidandla, V., Kalra, S.P., 1997. Velocity field in turbulent subcooled boiling flow. ASME J. Heat Transf. 119, 754–766.

Situ, R., Hibiki, T., Sun, D., Mi, Y., Ishii, M., 2004. Flow structure of subcooled boiling flow in an internally heated annulus. Int. J. Heat Mass Transf. 47, 5361–5364.

Smits, A.J., Muck, K.C., 1984. Constant temperature hot-wire anemometer practice in supersonic flows. Exp. Fluid. 2 (1), 33–41.

Stevens G.F., Kirby G. J., 1964, A quantitative comparison between burnout data for water at 1000 psia and freon-12 at 155 psia uniformly heated round tubes, vertical up-flow, United Kingdom Atomic Energy Authority, Report Number AEEW-R327.

Tagawa, M., Shimoji, T., Ohta, Y., 1998. A two-thermocouples technique for estimating thermocouple time constant in flow with combustion: In situ parameter identification of a first-order lag system. Rev. Sci. Instrum. 69 (9).

Todreas, N., Kazimi, M.S., 1990. Nuclear Systems I : Thermal Hydraulic Fundamentals. Hemisphere Publishing Corporation.

Wroblewski, Donald E., Eibeck, Pamela A., 1991. A frequency response compensation technique for cold wires and its application to a heat flux probe. Exp. Therm Fluid Sci. 4 (4).

Yun, B.J., Uhn, E.B., Bae, D.J., Song, C.H., 2010. Experimental investigation of local two-phase flow parameters of a subcooled boiling flow in an annulus. Nucl. Eng. Design 240, 3956–3966.

Zagarola, M.V., Smits, A.J., 1998. Mean-flow scaling of turbulent pipe flow. J. Fluid Mech. 373.